Delft University of Technology

Influence of free-stream turbulence on cycling aerodynamics

J. Raghavaraju

TU Delft

Influence of free-stream turbulence on cycling aerodynamics

by

Jahnavi Raghavaraju

to obtain the degree of Master of Science
at the Delft University of Technology.
to be defended publicly on Tuesday June 27, 2023 at 14:00.

Student number:	5312523	
Project duration:	December, 2021 – June, 2023	
Thesis Committee:	Dr. ir. BW. van Oudheusden,	TU Delft, chair of assessment committee
	Dr. A. Sciacchitano,	TU Delft, daily supervisor
	Dr. ir. W. Terra,	TU Delft, supervisor
	Dr. C. Morton,	AeroLab Tech, supervisor
	Dr. D. Ragni,	TU Delft, committee member

TU Delft

Preface

Moving to a new country right in the middle of a world-wide pandemic, to pursue my Masters in Aerodynamics (something I have been wanting to do for many, many years) has been one of the most absurd decisions I have made in my entire life. The journey through this Masters program has not always been easy. But now that I have made my way to the other side, I have to admit that I have absolutely no regrets.

This thesis would not have been possible without the most incredible supervisors any student could ask for - Andrea Sciacchitano, Wouter Terra, and Chris Morton. I would like to express my sincerest gratitude to them for their guidance in navigating the world of research in Sports Aerodynamics, I enjoyed every step of the process immensely. What sets them apart for me, from any good supervisor, is their kindness and understanding beyond the academic world, specifically through my struggles with mental health. Thank you, I could not have reached this point without your help. I would also like to express my special thanks to Peter Duyndam and Dennis Bruikman for patiently helping me with every single request of mine. I also thank Frits Donker Duyvis for his help with my experiments.

To my parents and my friends. I truly cannot attempt to explain how much your unwavering support has meant to me. I am incredibly grateful to my parents, Indira Kondur and Sreedhar Raghavaraju - I would not be here if not for your never ending faith in my decisions. My best friends from home, Supraja, Rakshana, Jeffrey, Sai, Shreya, you have been incredible since the time I met you. Distance never stopped me from feeling the love and support I have received from you throughout this journey, through the highs and lows. To the friends I found in Europe, who have now wormed their way into my life to become people I consider my family in Europe, Shreya, Sachin, Siddhy, I cannot imagine how my life would have turned out if not for you. My aero friends Aniruddha, Aaron, Josee, thank you for being great through this Masters journey, studies and otherwise. And finally, to absent friends. This one is for you.

J. Raghavaraju
Delft, June 2023

Abstract

Wind tunnel investigations of cycling aerodynamics are conducted in air streams that are designed to have minimum turbulence. This is not representative of the true, turbulent wind environment encountered by a track cyclist in an indoor velodrome. The goal of this thesis, broadly speaking, is to assess the effects of this turbulence on cycling aerodynamics.

To address this question, two experimental campaigns were conducted. The first consisted of track measurements, to measure the turbulence intensities and spectra encountered in an indoor velodrome, by an isolated cyclist and by a cyclist in the far wake of another. This turbulence data was collected using a three-hole pressure probe. In the case of an isolated cyclist, it was observed that the airflow was dependent on the cyclist's location on track. A spectral analysis also revealed the presence of periodic components to the airflow, a result of the cyclist's cadence. When riding in the far wake of another cyclist, the turbulence encountered was stronger when the distance of separation got smaller.

The second experimental campaign was conducted in the wind tunnel. First, the measured track turbulence intensities and spectra were simulated using grids, for small scale, high frequency turbulence, and large obstacles, for large scale, low frequency turbulence. Once the simulated turbulence matched the track turbulence to acceptable levels, its effects on the drag of a cylinder model, representative of the cyclist's limb, were assessed. These drag measurements were conducted using an external force balance. It was found that for a smooth surfaced cylinder, free-stream turbulence was enough to trigger flow transitions and cause a reduction in the measured drag. For a rough surfaced cylinder, increasing the turbulence triggered flow transition earlier, and led to an increased Reynolds number range for the critical flow regime. It was also seen that large scale turbulence did not have a significant effect of the drag of the cylinder.

Contents

List of Figures

List of Tables

Nomenclature

Acronyms

CFD	Computational fluid dynamics
CTA	Constant temperature anemometry
DP	Dropped position
FST	Free stream turbulence
HDV	Heavy-duty vehicle
HWA	Hot-wire anemometry
LDV	Laser doppler velocimetry
MAV	Micro-air vehicle
PIV	Particle image velocimetry
PSD	Power spectral density
RTS	Road turbulence system
TTP	Time trial position
UCI	Union Cycliste Internationale
UP	Upright position

Symbols

k	Roughness factor
α	Flow direction
β	Porosity
κ	Wave number
Λ_L	Streamwise integral length scale
Λ_T	Transverse integral length scale
λ_T	Taylor microscale
ν	Kinematic viscosity

ρ	Density
θ	Angular distance
A, B, n	King's law coefficients
A	Surface area
C_D	Drag coefficient
C_F	Force coefficient
C_M	Moment coefficient
D	Width of a bluff body
d	Thickness of peaks/troughs of a fabric
d	Wire/bar width
$E(\kappa)$	Turbulent energy spectrum
e	Turbulent kinetic energy
E_W	Voltage
f	Vortex shedding frequency
F_D	Drag force
I_W	Current
k_s	Roughness height
L	Length of protrusions
M	Mesh length
p	Static pressure
p_∞	Free stream static pressure
p_{tot}	Total pressure
r	Roughness coefficient
R_W	Resistance
R_{ij}	Autocorrelation function
Re	Reynolds number
St	Strouhal number
T_f	Fluid temparature

T_W	Wire temperature
TI	Turbulence intensity
u'	Streamwise velocity fluctuation
U_∞	Free stream velocity
U_θ	Velocity at a point on the surface
W	Width of protrusions
x	Downstream distance

1

Introduction

The 2016 track cycling sprint at the Rio Olympics saw Kristina Vogel win the gold medal with only 0.004 seconds ahead of her competitor. These small, but race-winning time differences are fairly common in elite cycling events, making aerodynamic optimisation an essential part of cycling races. Ninety percent of the resistive forces experienced by a cyclist in motion is accounted for by the aerodynamic drag [35], out of which about 80% is due to the rider itself and the remaining is from the bike and other components [29]. This implies that the greatest gains in performance is achieved through optimising the aerodynamics of the body, more specifically, the cycling position of the rider. Kyle et al. proposed the following hierarchy for reducing the aerodynamic resistance of the cyclist : position of the rider; cycling equipment; and minimising the rolling resistance and drive train friction losses [35]. Further reductions in aerodynamic drag can be achieved by riding closely in the wake of another cyclist, commonly referred to as ”drafting”. Drafting is common practice in group cycling events, and there has been extensive experimental and computational research conducted to quantify the drag reductions achieved through this practice [10][29][9][24][19][37].

It is apparent that there are numerous avenues of research one could venture into in the field of cycling aerodynamics. This particular thesis explores the aerodynamic optimisation of cycling skin-suits. Cycling suits have evolved from the simple cotton and wool jerseys of the late 19th century, to the advance apparel design involved in the Nike Swift Spin project [37][13]. This design consisted of up to five fabrics of different roughness used on different parts of the cyclist's body, based on the type of flow that is generally observed over that specific body part. With this design, the new time trial skin-suit provided a 3.9% reduction in drag at 53 km/h compared to the 2001 time trial cycling suits [13]. Aerodynamically efficient skin-suits essentially provide the cyclist with additional drag savings, with no extra effort on their part. The fabrics used to make such skin-suits are first tested using cylinder models. This simplifies the wind tunnel investigations, and is an acceptable method for fabric testing due to the fact that the human body can be approximated as cylindrical cross-sections for the ease of measurements [16].

The wind tunnels offer a controlled stream of air in which the turbulence levels are kept very low. While this is convenient for testing, this is not a true representation of the wind environment encountered by cyclists. Competitive cycling has developed

to include several different types of the sport - broadly classified into road cycling, off-road cycling and track cycling [60]. Track cycling, in particular, is a section of this sport that involves various formats of races taking place on a banked, oval track known as a velodrome. The rules of these track cycling events are set by the Union Cycliste Internationale (UCI), with regulations in place that cover every aspect of the sport - race formats, track design, and equipment design [59]. The atmosphere in an indoor velodrome is controlled with air-conditioning systems designed to keep the air speed below 0.25 m/s at the track level. While this ensures that the air encountered by the cyclist is less turbulent than in outdoor events, turbulence cannot be completely ignored. In an indoor environment, the flow field is turbulent due to the air conditioning systems, natural or forced convection due to the body heat and movement of cyclists and spectators, and the wakes generated by the movement of the cyclists [27]. This implies that the results of wind tunnel investigations are bound to deviate from the actual forces experienced by a cyclist. This thesis aims to measure the turbulent environment experienced in a velodrome in order to provide improvements to wind tunnel investigations of skin-suits.

Track cycling events are further divided into sprint and endurance events, and one such endurance event is the individual pursuit. Revisiting the fact that wakes of cyclists contribute to the turbulent environment of the velodrome, this thesis also looks to address the turbulence encountered by a cyclist in an event such as the individual pursuit. The individual pursuit involves two cyclists starting on opposite ends of the track racing to finish in the fastest time, or to catch the other cyclist. This format leads to either cyclist riding in the far-wake of the other. While drafting cyclists have been investigated quite thoroughly in the past [10][29][9][24][19][37], literature on effects of riding in the far-wake on drag reductions is quite minimal [11].

This leads us to the objective of this research : **”What are the effects of the turbulence levels measured in an indoor velodrome on the aerodynamic drag of a cyclist?”**

The remainder of this thesis is structured as follows. A review of the relevant literature on cylinder aerodynamics, cycling aerodynamics and turbulence simulation in a wind tunnel is presented in chapter 2. This chapter is concluded with a statement of the research questions to be addressed in this thesis. Chapter 3 provides a background of the measurement techniques employed in this thesis. Chapter 4 discusses the Velodrome set up and procedures, followed by the wind tunnel set up and procedures in Chapter 5. Chapter 6 deals with the results of the two experimental investigations. Finally, chapter 7 concludes the thesis with a summary of the findings and recommendations for future work.

2

Literature review

2.1. Bluff body aerodynamics

A bluff body is one that is characterised by large regions of separated flow and high aerodynamic drag [48]. These bluff bodies exhibit dramatic reductions in their width towards their trailing edge which impose a large adverse pressure gradient on the boundary layer, resulting in these flow separations that may or may not reattach to the surface of the body [54]. The flow around such bodies exhibits transitions from laminar to turbulent and these are influenced by several parameters. These transitions occur as a series of transition states that occur over a range of Reynolds numbers, and are sensitive to small disturbances, such as the free stream turbulence, surface roughness, aspect ratio of the body, end effects and others [48]. The Reynolds number, *Re*, is defined as the ratio of inertial and viscous forces experienced by the body, and can be mathematically expressed as given in equation 2.1.

$$Re = \frac{U_\infty D}{\nu} \tag{2.1}$$

where U_∞ is the free stream velocity, D is the width of the bluff body and ν is the kinematic viscosity of the fluid [54]. The separation of the flow from the body creates a wake, which is a region of low-velocity flow behind the body. The wake of bluff bodies is characterised by vortex formation and shedding, and this shedding frequency *f* is defined by the Strouhal number *St* given in equation 2.2

$$St = \frac{fD}{U_\infty} \tag{2.2}$$

The drag force on a body generally comprises of the skin-friction drag and the pressure drag, but for a bluff body, the drag force experienced is predominantly due to the pressure drag. This pressure drag is due to the difference between the high pressure region around the stagnation point of the body and the low pressure region in the wake of the body [54]. The non-dimensional drag coefficient C_D can then be defined as a ratio of the drag force F_D to the dynamic pressure $\frac{1}{2}\rho U_\infty^2$ (where ρ is the fluid density) and the surface area A, mathematically expressed in equation 2.3.

$$C_\mathsf{D} = \frac{F_\mathsf{D}}{\frac{1}{2}\rho U_\infty^2 A}, \tag{2.3}$$

While there exists several types of bluff bodies, the study of flows around circular cylinders is the one that is relevant to this thesis. This is because it is possible to simplify the human body to a series of interconnected cylinders sometimes, as described by Chowdhury et. al [17]. This simplification is helpful in the study of aerodynamics of athletes, to understand the basic flow topology and the effects of disturbances such as free stream turbulence and surface roughness, which can later be extended to complex, three-dimensional objects such as a cyclist.

2.1.1. Flow around a circular cylinder

A flow around a circular cylinder can be described by different flow states that occur over a range of Reynolds numbers : fully laminar *L*, a series of transition states T_r, or fully turbulent *T* [65]. These transition states can be categorised into four separate flow states based on the location of transition. A pictoral representation of these four transition states can be found in figure 2.1. In the first of these transition states, figure 2.1 (a), the laminar vortices in the wake of the cylinder become turbulent due to disturbances further downstream. With increasing Re, this turbulence spreads upstream while the free shear layers around the near-wake remain laminar. These free shear layers are the next to undergo transition, forming the second transition state seen in figure 2.1 (b). When Re increases further, the transition region moves upstream to the separation point (figure 2.1 (c)). The third transition state is a result of a complex interaction between the separation and transition, resulting in fully turbulent boundary layers along the separation line. The final flow state is characterised by transition in boundary layers away from the separation point, as in figure 2.1 (d), whose upstream movement with increasing Re eventually reaches the stagnation point of the cylinder [65].

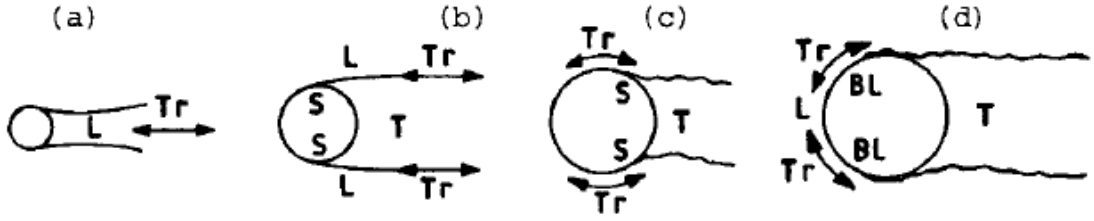

Figure 2.1: Transition flow states for a smooth circular cylinder. (a) Transition in the wake ; (b) Transition in free shear layers ; (c) Transition at separation ; (d) Transition in boundary layers [65]

These transition flow states can be further classified based on the distinct flow patterns that occur over a specific range of Re, referred to as ”flow regimes” [65]. The changing flow patterns in turn cause changes in the mean and fluctuating forces exerted on the cylinder. Roshko [47] offers a relatively simple classification of the flow regimes, represented in a plot of the drag coefficient C_D vs Re in figure 2.3 [65]. The sub-critical regime ($Re = 300$ to 2×10^5) is characterised by a laminar boundary layer over the circumference of the cylinder until the point of separation at an angle of about 80° from the upstream stagnation point, which results in a wide wake. Here, the C_D is relatively high, and more or less independent of the Reynolds number, and has a value of 1.2 [47]. The wake of the cylinder in the subcritical regime is characterised by

a turbulent vortex street consisting of strong, periodic vortex shedding, with a constant St of about 0.2 [23].

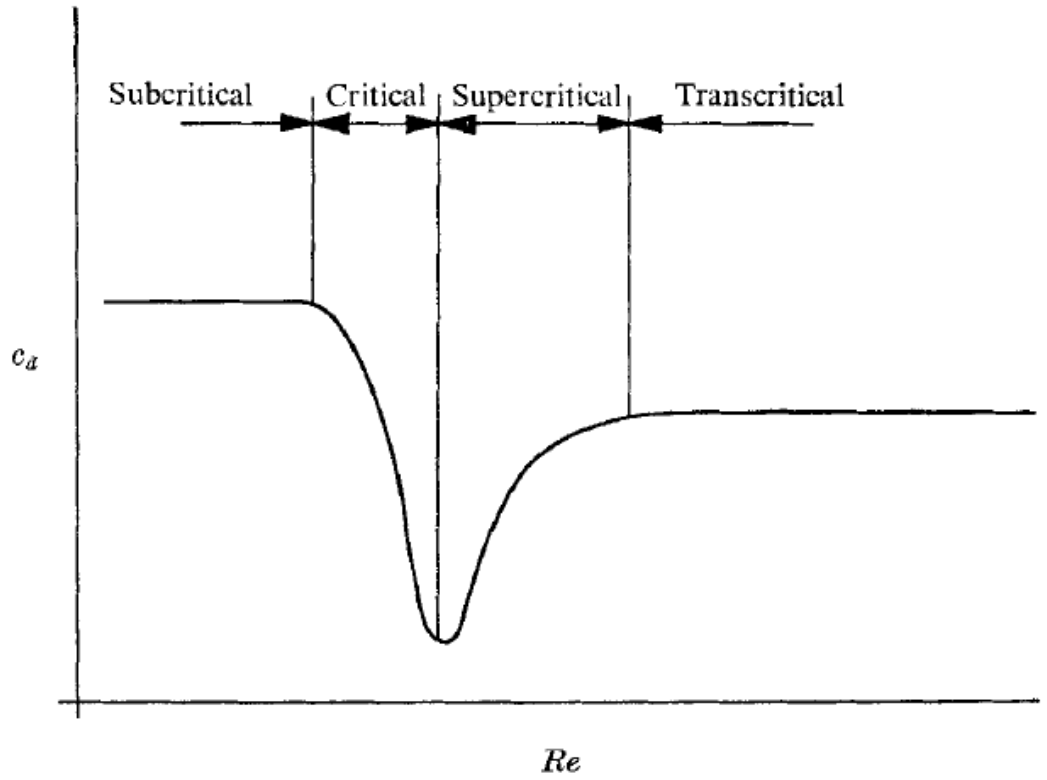

Figure 2.2: The four flow regimes defined by Achenbach [1]

The critical regime, between $Re = 2 \times 10^5$ to 1×10^6, is defined by the formation of a laminar separation bubble which shifts the final separation point to an angle of 140° from the stagnation point, resulting in a narrow wake and reduced C_D around 0.8. The end of the critical regime is marked by the Re at which the C_D reaches its lowest, a phenomenon commonly referred to as the *'drag crisis'* [15]. The critical regime is extremely sensitive to disturbances. At drag crisis, the St jumps abruptly from 0.2 to 0.46 [23]. It was found that the wake consisted of quasi-regular flow fluctuations. In between the subcritical and the critical St, only two intermediate values of St were found to exist, and these were attributed to the occurrence of a separation bubble on only one side of the cylinder [2].

This is followed by the supercritical regime ($Re = 1 \times 10^6$ to 5×10^6) where the C_D is increasing again [47]. In this regime, the bubble shrinks with increasing Re until it is suppressed. The vortex shedding in the wake is also suppressed in this regime [47]. The St was found to decrease stepwise from a value of 0.5 at Re $= 1.5 \times 10^6$ to about 0.25 at Re $= 4 \times 10^6$ [2].

The fourth and final flow regime is the transcritical regime ($Re > 5 \times 10^6$), where the bubble no longer exists and the separation becomes turbulent. The value of C_D is nearly constant and lower than that of the subcritical regime. Vortex shedding reappears in this regime [47] and the St number is more or less invariant [2]. A more extensive classification of the flow regimes is presented in Zdravkovich [65], with a

total of 15 flow regimes covering the laminar, transition and turbulent flow states.

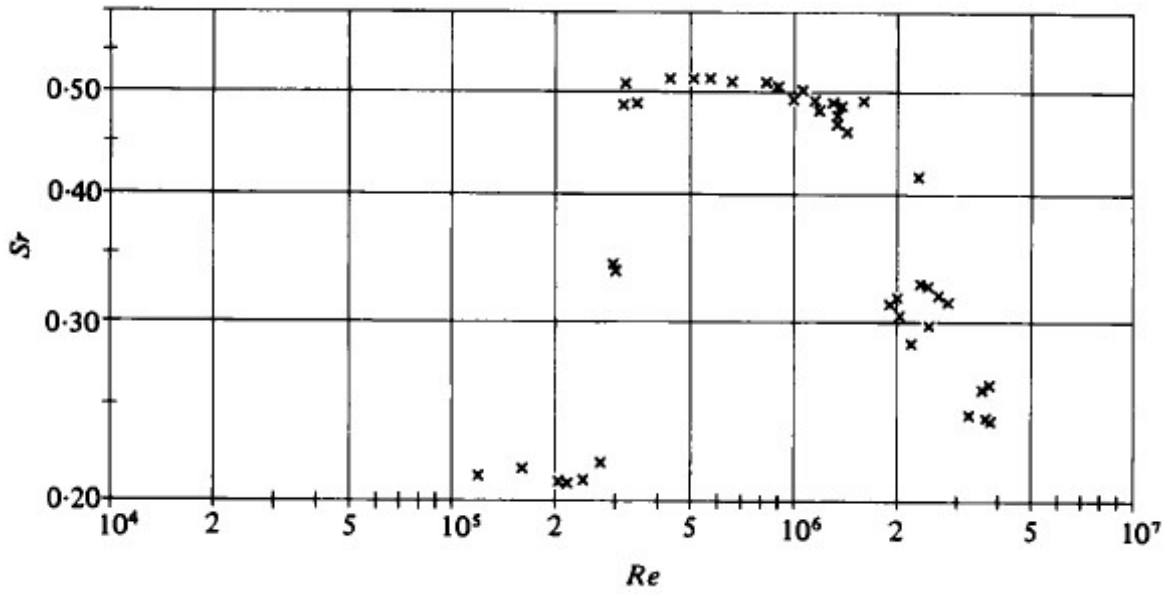

Figure 2.3: Strouhal number St (Sr here) vs Reynolds number Re for a smooth cylinder [1]

2.1.2. Effects of free stream turbulence

Free stream turbulence (FST) refers to the random three-dimensional velocity fluctuations present in every fluid stream [8]. It can be quantified by its turbulence intensity, length scales, and spectral composition. The turbulence intensity, given in equation 2.4, is defined as the ratio of the root-mean-square velocity fluctuations of the stream-wise velocity component, $u^{'}$, to the mean velocity of the flow, U_{∞} [45]. It is a measure of the intensity of the velocity fluctuations of the wind.

$$TI = \frac{\sqrt{\overline{u^2}}}{U_{\infty}} \tag{2.4}$$

The energy of the turbulent flow is spread over a broad frequency band. To gain a better understanding of this flow field, it is necessary to also examine the entire spectrum of energy [46]. The turbulent kinetic energy *e* is related to the turbulent energy spectrum $E(\kappa)$ as given in equation 2.5. Here, κ represents the wave numbers, and $E(\kappa)$ gives the distribution of energy over these wave numbers [64].

$$e = \int_0^{\infty} E(\kappa) d\kappa \tag{2.5}$$

The length scales of turbulence offer information on the size of the eddies in a turbulent flow. There are three important length scales used to define such a flow - the integral length scale, Taylor micro scale and the Kolmogorov scale. The first two length scales mentioned are obtained from spatial two-point correlations of the velocity field. In the stream-wise direction, the autocorrelation function $R_{ij}(r,t)$ is defined as in equation 2.6, where *u'* represents the turbulent velocity fluctuation [45].

$$R_{ij}(r,t) = \left\langle u_i'(x_1,t)u_j'(x_2,t)\right\rangle \tag{2.6}$$

The integral length scale is representative of the average size of the largest, most energetic turbulent eddies. The streamwise and transverse integral length scale, Λ_L and Λ_T, are given in equation 2.7. Here, R_{11} and R_{22} are the one-dimensional correlation functions of the velocity in the streamwise and transverse directions [64].

$$\begin{aligned}\Lambda_L &= \frac{1}{\overline{u'^2}}\int_0^\infty R_{11}\left(r_1\right)dr_1 \\ \Lambda_T &= \frac{1}{\overline{u'^2}}\int_0^\infty R_{22}\left(r_1\right)dr_1\end{aligned} \tag{2.7}$$

Fage et al. [25] studied the effects of FST on the drag of a circular cylinder. In this work, turbulence was produced using a mesh placed in the wind tunnel. Drag measurements were conducted on the cylinder placed at various downstream distances from the mesh which allows for measurements in a turbulent flow of decreasing intensity. The results from this investigation, a plot of the drag coefficient vs the logarithm of Re reproduced in figure 2.4, shows that increasing turbulence intensity leads to a shift in the drag curve towards lower Re as opposed to measurements conducted in a turbulence free flow. In this figure, *S* refers to the distance between the mesh and the cylinder model [25]. It can be seen that free-stream turbulence does not cause a change in the shape of the C_D vs Re curve. An extension of these results to include various bluff bodies under turbulent flows were presented by Bearman and Morel [8]. It was concluded that the interaction of the FST with the flow over the bluff bodies involves three basic mechanisms which produce an overall effect on the drag of the bluff body. These are accelerated transition to turbulence, enhanced mixing and entrainment, and distortion of the FST by the mean flow [8].

The ratio of the absolute integral length scale to some characteristic dimension of the flow feature under study is a more important parameter than the length scale by itself. In the case of flows around bluff bodies, the main effect of turbulence is its influence in the development of multiple separated shear layers, and their interaction with each other. This means that a characteristic dimension of the body itself is an appropriate choice for study [8]. When the integral length scale is very large when compared to the body dimension, the longitudinal velocity fluctuations will be seen as slow changes in the mean wind speed and the lateral fluctuations will be perceived as slow changes in the direction of the wind [7]. If the integral length scale of FST is very small, the FST is distorted by the cylinder such that certain components of the FST are amplified, and others, attenuated [8][7].

Small-scale turbulence in the flow encourages early transition in the flow over the cylinder and a delay in separation. This turbulence leads to a lower transition Re, and the decrease in C_D occurs sooner [34], as seen in figure 2.4. After reaching the minimum value of C_D, the C_D sharply increases due to flow transition occurring on both sides of the cylinder. With further increase in Re, the C_D increases until it reaches a constant value in the transcritical flow regime [34]. The angle of flow separation in the subcritical regime is delayed to 120° while the critical regime exhibits a separation angle of 135°, similar to the supercritical regime observed in a smooth flow. This flow condition lasts over a small range of Re, after which the flow separation

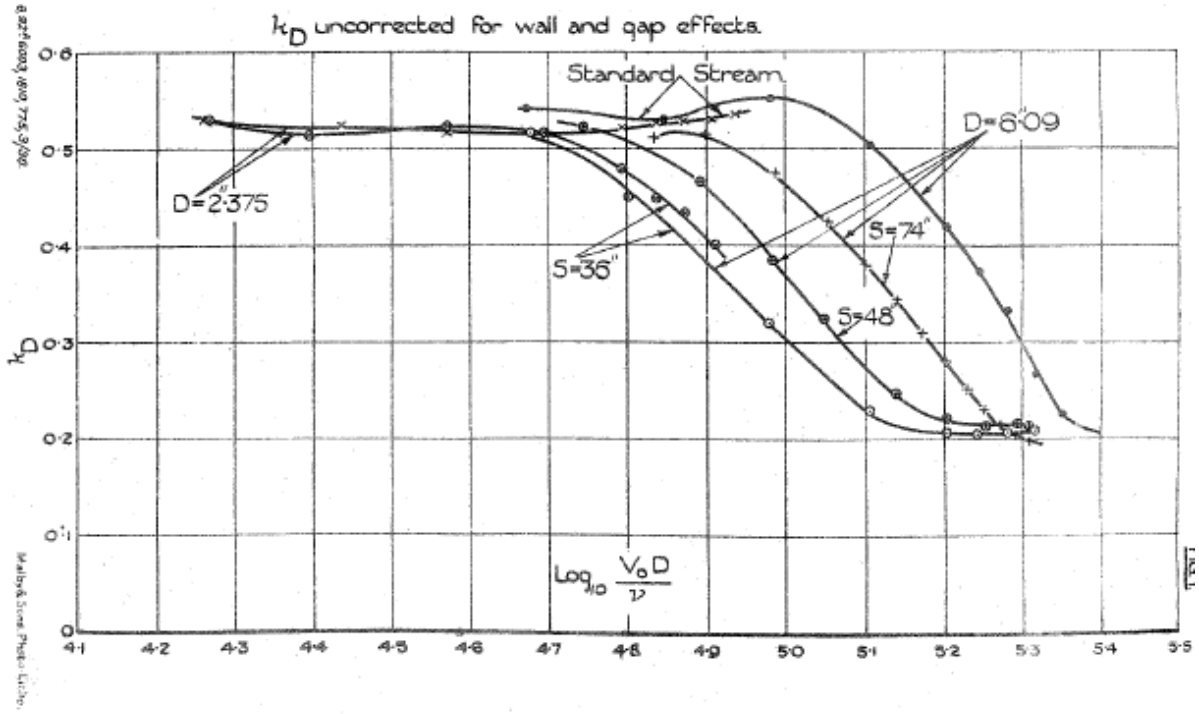

Figure 2.4: Effects of free stream turbulence on C_D vs Re for a circular cylinder[25]

shifts to 115°. This value is similar to the case of flow separation at very high Re in smooth flow. This implies that the small scale turbulence effectively raises the Re of the flow [34]. A possible explanation for these results is that the FST is selectively amplified due to vortex stretching as the mean flow approaches the stagnation zone of the cylinder, known as the vortex amplification theory [49]. The experimental results of Kwok mentioned above offer a verification of this theory [34].

2.1.3. Effects of surface roughness

Surface roughness of a cylinder is quantified by a roughness coefficient $\frac{k_s}{D}$, which can be defined as the ratio of the roughness height to the width of the cylinder [1]. Figure 2.5 reproduces a plot of the drag coefficient C_D against the Reynolds number Re for a circular cylinder of varying surface roughness from the investigations of Achenbach [1]. This research revealed that while the surface roughness does not affect the drag of the cylinder, or the Strouhal number in the subcritical regime, it plays a role in the drag crisis phenomenon and St observed in the critical flow regime. In the critical regime, the location of the final separation point occurs at a lower angle of separation as compared to a smooth surfaced cylinder [2]. Increasing surface roughness shifts the critical Re to lower values, and the drag drop from the sub-critical to the critical regime occurs faster [42]. The range of critical Re is also shrinking [2]. As surface roughness increases, the minimum C_D increases, while the corresponding St decreases [2].

In the critical and supercritical regimes, the behaviour of St is dependent on the relative roughness of the surface. At smaller values of roughness, the vortex shedding mechanism is not stabilised as in the case of higher Re or higher roughness. The

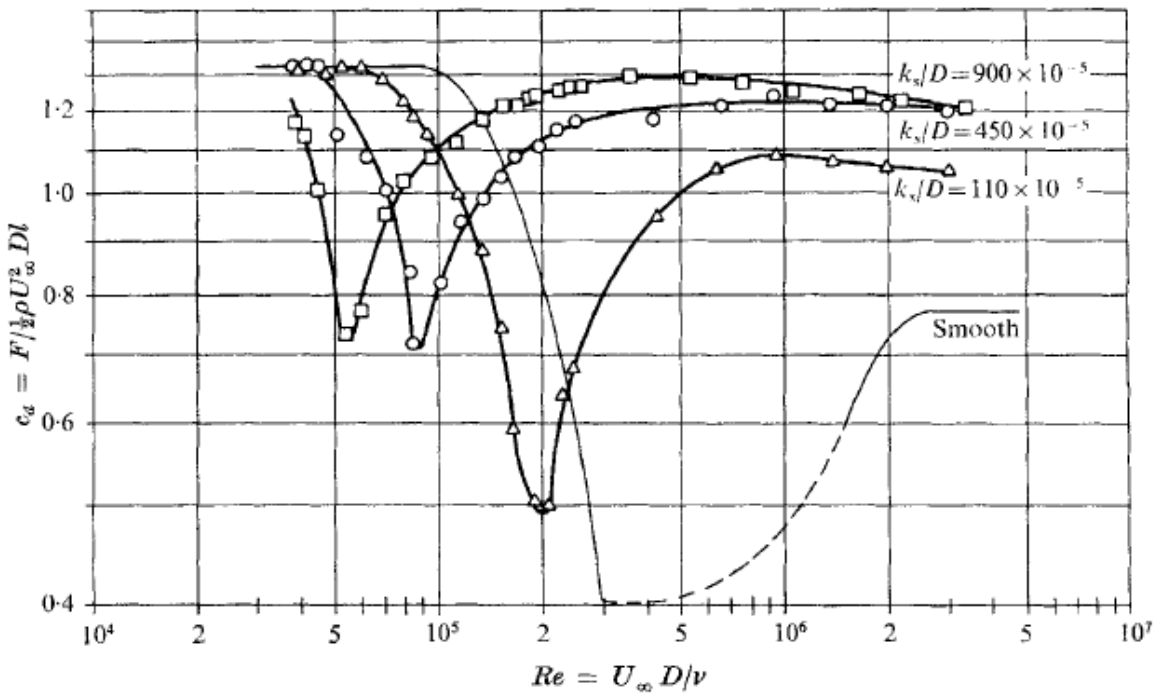

Figure 2.5: Effects of surface roughness on C_D vs Re for a circular cylinder[25]

sensitivity of the flow to disturbances leads to random regions of critical or subcritical flow, with the flow exhibiting different values of St at these regions [2]. As Re is increased further in the supercritical regime, C_D grows until reaches a near constant value in the transcritical regime. In the supercritical regime, the flow transitions from laminar to turbulent, and the intermediate laminar separation that is seen in the critical regime is absent. The location of transition moves upstream with increasing Re [2]. In the transcritical regime, the value of C_D was found to increase with increasing surface roughness [1]. The St is weakly dependent on the Re, and its dependence on roughness could not be ascertained [2].

2.2. Cycling aerodynamics

The interaction of a cyclist with the surrounding air gives rise to aerodynamic forces that are experienced by the cyclist. The cyclist is subjected to three aerodynamic forces and three aerodynamic moments, typically defined in the frame of reference of the cyclist's body, which are depicted in figure 2.6.

The three forces, lift force F_L, drag force F_D, side force F_S, and the three moments defined about the centre of the wheelbase, pitching moment M_P, roll moment M_R and yaw moment M_Y can be described by their respective force and moment coefficients [19]. These are represented in equation 2.8. These coefficients are normalised by the dynamic pressure $\frac{1}{2}\rho U_\infty^2$ and frontal area *A*, with the moment coefficients also including the wheelbase length *l*.

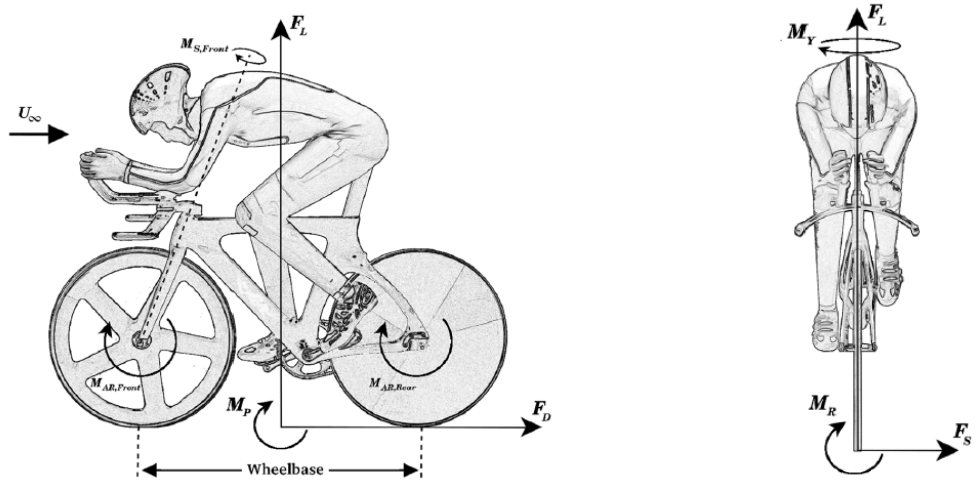

Figure 2.6: Aerodynamic forces and moments experienced by a cyclist [19]

$$C_{\text{F:D,S,L}} = \frac{F_{\text{D,S,L}}}{\frac{1}{2}\rho U_\infty^2 A},$$
$$C_{\text{M:P,R,Y}} = \frac{M_{\text{D,S,L}}}{\frac{1}{2}\rho U_\infty^2 A l}. \tag{2.8}$$

Cyclists fall under the category of bluff bodies, which means that the largest source of aerodynamic resistance in the case of cycling is from pressure drag, as is the case for bluff bodies. In order to make gains in performance, it is important to minimise the drag experienced by the cyclist. The rest of this section delves into the flow topology of a cyclist, and methods of drag reduction in the case of an isolated cyclist, specifically with respect to skin-suits, and drag reductions that can be achieved by riding in the wake of an other cyclist.

2.2.1. Flow topology of a cyclist

The cyclist-bicycle system is a complex, three-dimensional geometry with moving components like legs, pedals and wheels [37]. The study of the flow topology of the cyclist is an important step to understand how and where the drag force is generated and thus provides a better way to come up with drag reduction techniques [20].

The flow around a cyclist is influenced by the position of the legs of the cyclist during the pedal cycle [20]. Wind tunnel investigations of a cycling mannequin on a bicycle in time trial position with static legs of Crouch et al. [20] and CFD simulations conducted by Griffith et al. [29] reveal the presence of two characteristic flow regimes based on the position of the cyclist's legs. In the symmetric, low drag flow regime, the crank angle was almost horizontal and the feet were nearly aligned. A pair of streamwise vortices originating from the upper hip and from the inner thighs led to a reduced wake size due to their symmetry and mutual interaction, and in turn led to lower drag. On the other hand, the case of the asymmetric, high drag flow regime observed when one leg was extended showed flow separations from the upper hip of the extended leg and the rear hip of the raised leg. The wake flow tended to shift towards one side and also persisted further downstream when compared to the low

drag regime. Additionally, in the asymmetrical regime, secondary vortex structures were identified behind the upper arms, elbows, helmet and calf of the cyclist.

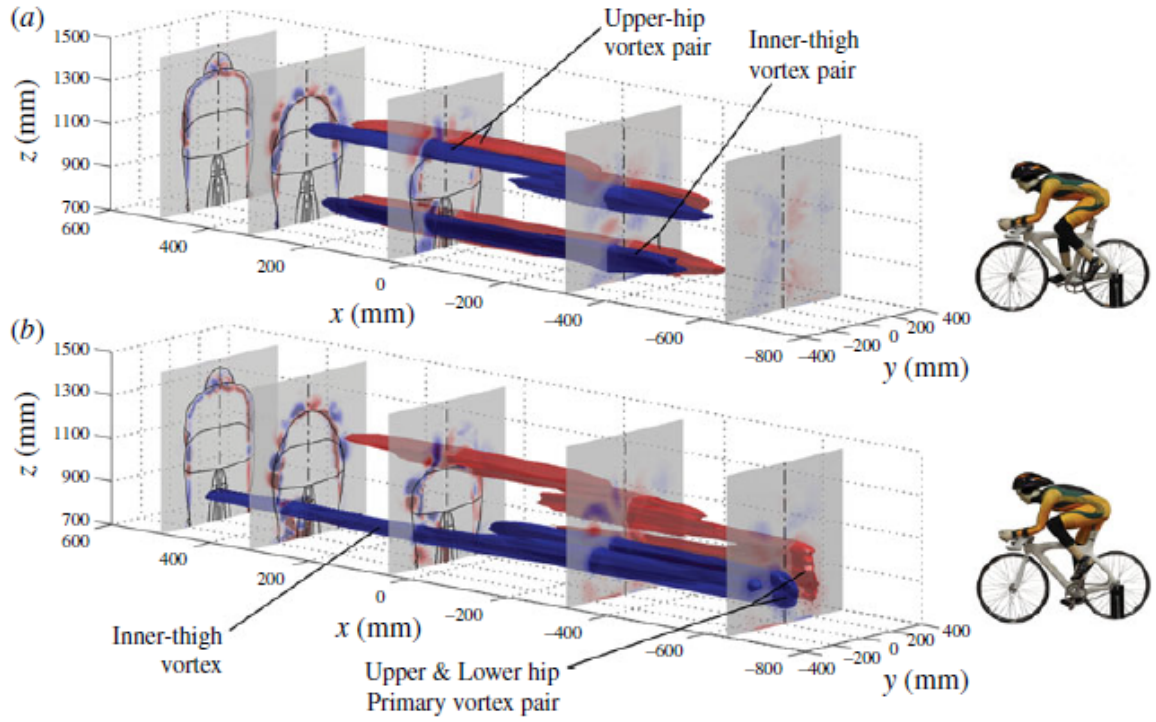

Figure 2.7: Spatial development of primary vortex structures for (a) symmetrical and (b) asymmetrical flow regime, from [20]. Blue represents clockwise rotation and red represents anti-clockwise rotation

The phenomenon of drag crisis, described in case of circular cylinders previously, also occurs along the body of a cyclist. This was investigated by Terra et al. [53] using robotic volumetric Particle Image Velocimetry on a cycling mannequin in time trial position for the asymmetrical flow regime. It was found that not only does the critical flow condition occur at different speeds for different locations of the leg due to its tapered geometry, it is also affected by other mechanisms. The drag crisis is affected by local streamwise vortices in the wake of the cyclist limb, as well as by the effect of interactions with the wakes from other body parts [53]. These results directly impact the aerodynamic optimisation of cycling skin-suits, and will be explored further in the following sections.

2.2.2. Single rider aerodynamics

Historically, drag reductions that can be achieved via the modification of the rider position have been extensively investigated, with the development of new positions and aerodynamic optimisation of existing positions. The time trial position has been found to have the lowest aerodynamic drag, followed by the drops position, upright brake hoods and stem positions in order of increasing aerodynamic drag. A detailed investigation of this is out of the scope of this thesis but can be referred to in literature [19] [37]. Further development of rider positions is limited by the strict regulations laid down by the UCI [59].

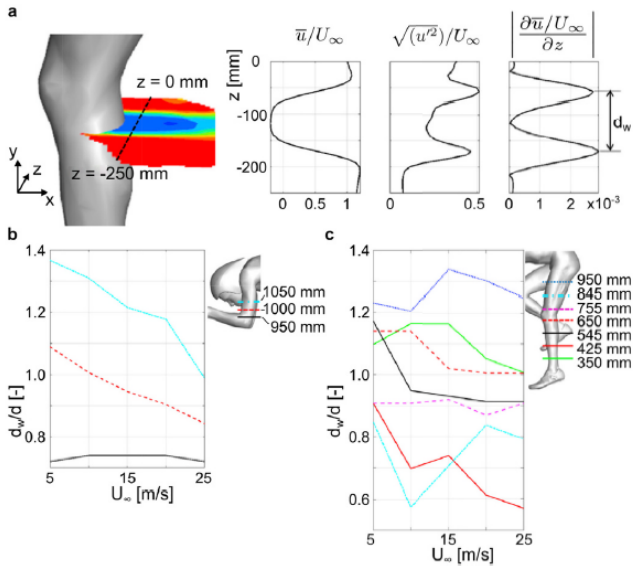

Figure 2.8: (a) Definition of the wake width d_w on a leg section as the distance between the peaks of the root mean square velocity fluctuation, or as the inflection points of the velocity profile. Wake width at different flow velocities U_∞ on the (b) upper arm (c) extended leg. Adapted from [53]

These UCI regulations also extend to the cycling equipment : the design of bicycle frames, wheels, helmets and skin-suits [59]. Nevertheless, streamlining the equipment for aerodynamic performance is a major design criteria for cycling at elite levels. Enhancing the aerodynamic performance of cycling equipment provides cyclists with gains in performance with no extra effort from the cyclists' part. The focus in this thesis will be on skin-suits of cyclist, and will be explored in detail next.

Skin-suits

For the ease of aerodynamic analysis, the body of a cyclist can be approximated as a series of cylindrical cross sections oriented at different angles with respect to the flow, based on the posture the cyclist assumes [16]. This is illustrated in figure 2.9. The description of the different angles can be found in table 2.1. This cylinder representation of cyclists is particularly useful in determining the efficiency of different fabrics, as a first step in the wind tunnel testing of skin-suits. The main idea behind the development and testing of skin-suits is to exploit the phenomenon of drag crisis [43].

Body segment angle	Road racing position °	Time trial position °
Thigh ($\alpha 1$)	0 - 115	0 - 115
Trunk ($\alpha 2$)	45	0
Arm ($\alpha 3$)	115	105
Forearm ($\alpha 4$)	115	0

Table 2.1: Angles of different body segments in Road racing and Time trial positions, reproduced from Chowdhury et al. [17]

Methods of drag reduction by modifying skin-suits of cyclists are dependent on

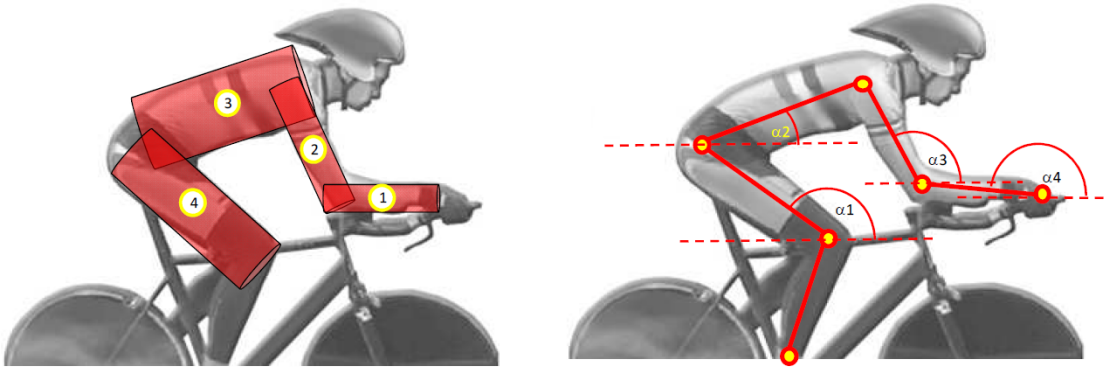

(a) Cylinder representation (b) Angles of a cyclist body parts

Figure 2.9: Cylinder representation and angles of a cyclist's body parts that are covered with fabric [16]

modifying the effective shape presented by the subject to the incoming air flow [12]. In the case of cycling, the drag force can be reduced by minimising the frontal area and the drag coefficient. The drag coefficient itself can be approximated as a function of the shape, motion and surface of the athlete [43]. The factors that influence skin-suit aerodynamics were summarised by Oggiano et al. [43]. A pictorial representation of these factors is reproduced in figure 2.10. While all these influencing parameters interact to result in a change in the drag force experienced, it is useful to examine them individually to determine the role they play in drag reduction.

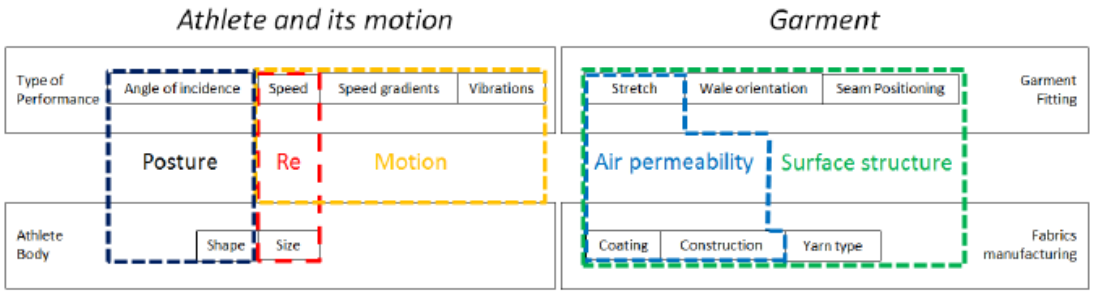

Figure 2.10: Factors that influence fabric characteristics [43]

When it comes to skin-suits, the frontal area can be reduced by utilising suits that offer a tight fit to the body of the cyclist. The effect of skin-suit size and wrinkling were examined by Brownlie et al. in the Nike swift spin project [13]. In order to do so, a full-scale wind tunnel test was conducted using a modern time trial bike fixed to a balance and cyclist as the test subject. Measurements were conducted at 40 kph, with the cyclist in an upright position. It was found that the drag increased by 6.3% between a small and extra large sized cycling jersey.

Fabrics designed for the purpose of aerodynamic optimisation may reduce the total drag force of the cyclist by minimising either the pressure or the friction drag [13]. The surface roughness of the fabric has been defined differently by different authors. Underwood et al. estimate the roughness by determining the thickness of the peaks and troughs, d, using a microscope, along with the length L, width W and distance

between protrusions to calculate a roughness factor *k* and roughness coefficient *r* [58]. These parameters are represented in equation 2.9. Oggiano et al. propose a model that represents roughness by macrostructure, microstructure and fuzziness of the material. The macrostructure represents the large modifications on the surface, the microstructure represents roughness induced by the knitting or warping process, and the fuzziness is determined by the type of yarn used [43].

$$\begin{aligned} k &= \sqrt{W \cdot d} \\ r &= \frac{k}{D} \end{aligned} \tag{2.9}$$

The surface roughness of the skin-suit fabric is an important parameter to be considered in the discussion on the state of the flow over the cyclist. The flow over a smooth human limb moving at a low speed is laminar at its leading edge, separating at the widest point on the limb creating a large low pressure wake. This laminar flow becomes turbulent at higher speeds, delaying the point of flow separation and thereby reducing the width of the wake. The drag force drops rapidly at a certain critical velocity, which, as stated previously, is termed as drag crisis. This drag crisis phenomenon can be triggered at a lower speed by using a fabric with a rough texture. On the other hand, the flow over the limb of the cyclist gives rise to shear forces, which are lower for a smooth surface than for a rough surface. As the speed increases beyond the point where smooth surfaces undergo drag crisis spontaneously, rough surfaces cause a turbulent boundary layer which produces additional skin friction drag. The range of speeds for which rough surfaces provide an aerodynamic advantage are thus limited [13].

Figure 2.11, reproduced from Brownlie et. al [13], shows the effect of fabric roughness on the drag coefficient at increasing Reynolds numbers. Fabric 1 was a very smooth stretch fabric and fabrics 4, 7, 40 have varying roughness, with 7 exhibiting the highest roughness. The details of these fabrics can be found in [13]. It can be seen that for a vertically oriented cylinder where pressure drag dominates, the drag crisis is triggered at different Reynolds numbers based on the surface roughness, illustrated in figure 2.11a. On the other hand, where skin friction drag dominates in the case of a horizontally oriented cylinder, smooth fabrics produce lower C_D.

The angle of incidence of the flow with respect to the body segments of a cyclist in a time trial and road racing position are summarised in table 2.1. Chowdhury et al. conducted drag measurements for cycling fabrics over a range of angle of attacks, in order to determine the forces on the different body parts of the cyclist [17]. The results have been reproduced in figure 2.12. Here, sample 4 refers to a smooth fabric, and sample 5 is a rough fabric. It is concluded that at a higher angle of attack, between 45° and 115°, the rough fabric undergoes flow transition earlier than the smooth fabric. At low angle of attack, 30°, the smooth fabric has a lower C_D value. This means that parts of the body aligned with the flow, like the torso of the cyclist in the time trial position, figure 2.9, can be covered in smooth fabric and body parts yawed to the flow direction can be covered in rough fabric to trigger transition at lower speeds. This is precisely the motivating factor behind the Nike Swift Spin suit used by several successful athletes, a zoned fabric suit made up of five different fabrics [13].

In addition to the surface roughness of the fabric, the position of seams of the

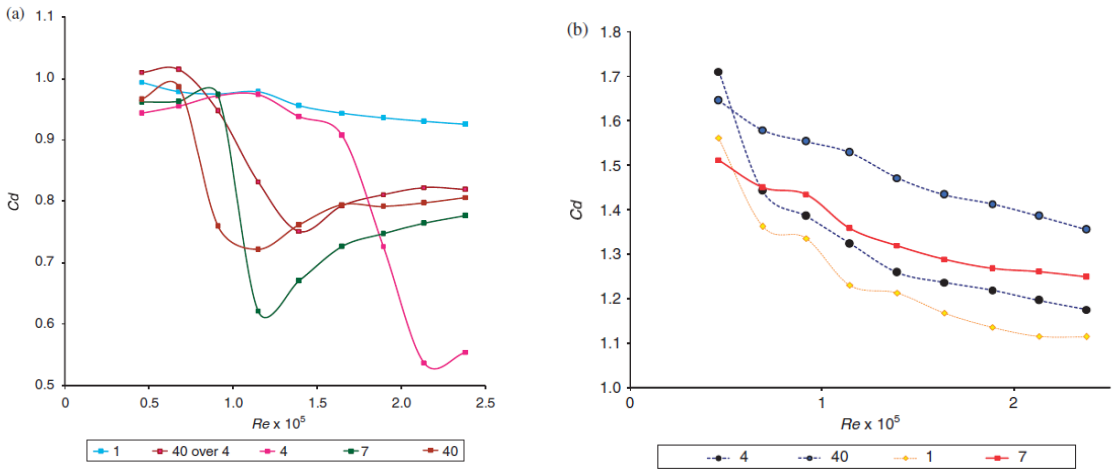

(a) Cylinder oriented vertically to the flow

(b) Cylinder oriented horizontally to the flow

Figure 2.11: C_D vs Re for fabrics of different roughness [13]

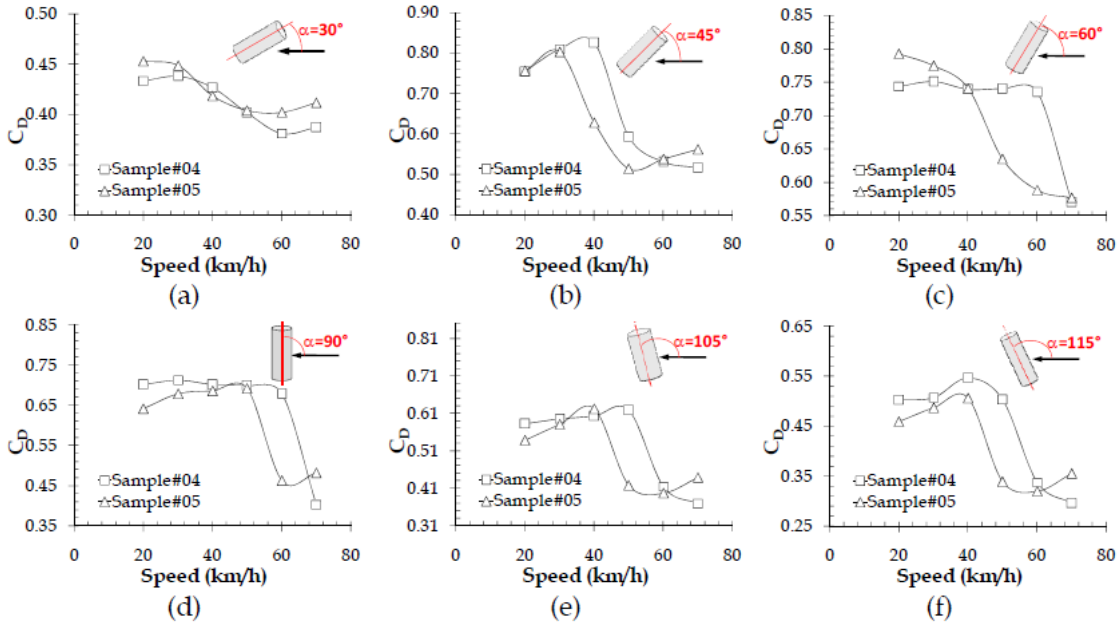

Figure 2.12: C_D vs Speed for cycling fabrics at different angles of attack [16]

fabric and fibre orientations of the material are also factors that should be considered to obtain further reductions in the drag of the cyclist. Underwood et al. [58] and Chowdhury [16] looked into the effect of seam placements and found that seams could trigger the flow transition earlier. A seam placed at 45° from the front centre of the cylinder led to an earlier flow separation when compared to other orientations. The research conducted by Chowdhury [16] also revealed that the orientation of the fabric stitch could have a small effect on the drag.

In the discussion thus far, the recurring theme has been the testing of fabrics using cylinders as a simplified representation of human body parts. This does not properly simulate the three dimensional flow around an athlete's limb, or the interaction of the flow around the multiple, interconnected limbs of the athlete [22]. In a study conducted

by D'Auteuil et al. [22], wind tunnel tests conducted on a 1:1 scale mannequin of an athlete in the side-push skating position investigated the effect of size and aspect ratio of limbs, as well as the three dimensional flow interactions. All these parameters were found to have significant effect on flow transitions over the athlete's body parts, as these must be taken into account to determine the appropriate skin-suit fabrics to be used. Similar observations have been made by Brownlie [12], and Chowdhury et al. [16] in the case of cycling skin-suits, who performed fabric tests using cylinders as well as full scale cyclist mannequins. The study on the drag crisis distribution of a cyclist by Terra et al. confirms the complex nature of flow transitions and drag crisis of a full cyclist model [53].

2.2.3. Drafting between two cyclists

Cyclists can also minimise their aerodynamic drag by *"drafting"*, which is riding in the wake of another cyclist. Both the lead rider and the trailing rider are found to have aerodynamic benefits from drafting. Blocken et al. propose the following to explain these drag effects following analysis of CFD simulations: the drag reduction of the trailing rider due to the presence of the lead rider is due to the decrease in overpressure in front of the trailing rider, as well as the reduction of the absolute value of underpressure at the back of the trailing rider. On the other hand, the trailing rider decreases the absolute value of the underpressure at the back of the lead rider, resulting in a drag reduction for the lead rider [10]. The extent of drag reduction on the two riders is dependent on a couple of parameters which will be explored below.

Results of an investigation by Edwards et al. showed that the drag of the trailing cyclist shows a greater reduction when the lead rider has a higher drag area, with a drag drop of 35.6%, 41.3%, 50.5% for a small, medium, large drag area of the lead cyclist respectively [24]. Blocken et al. analysed the effects of drafting in three different rider positions - upright (UP), dropped (DP) and time trial (TTP) positions using CFD simulations supported by wind tunnel measurements. The drag area of the cyclist varies based on the rider position, with the upright position having the maximum drag area and the time trial position having the lowest. When comparing the results of a single rider with two drafting cyclists at a separation of 0.01 m, it was found that the drag reduction of the trailing cyclist is 27.1%, 23.1%, 13.8% and that of the leading cyclist is 0.8%, 1.7%, 2.6% for UP, DP, TTP respectively [10]. Pressure coefficient plots of these different cases are reproduced from Blocken et al. in figure 2.13.

The axial separation, or wheel-to-wheel distance between the two cyclists is inversely proportional to the drag reduction in both the lead and the trailing riders. The largest drag savings is obtained when there is almost no gap between the two riders. This is confirmed by the CFD simulations of Blocken et al. [10], the wind tunnel tests of Barry et al. [6] as well as the on-site Ring-of-Fire measurements by Spoelstra et al. [50]. Some variations in the percentage drag reductions between the different studies are to be expected due to variations in testing conditions, or simplifications undertaken to simply the testing. The lateral separation between the two cyclists also has a similar effect on the drag savings of the riders, with the largest drag reductions obtained when there is no lateral separation between the riders. Results from the wind tunnel investigations of Barry et al. are reproduced in figure 2.14.

The effects of cross-wind were analysed by Bellioli et al. via wind tunnel mea-

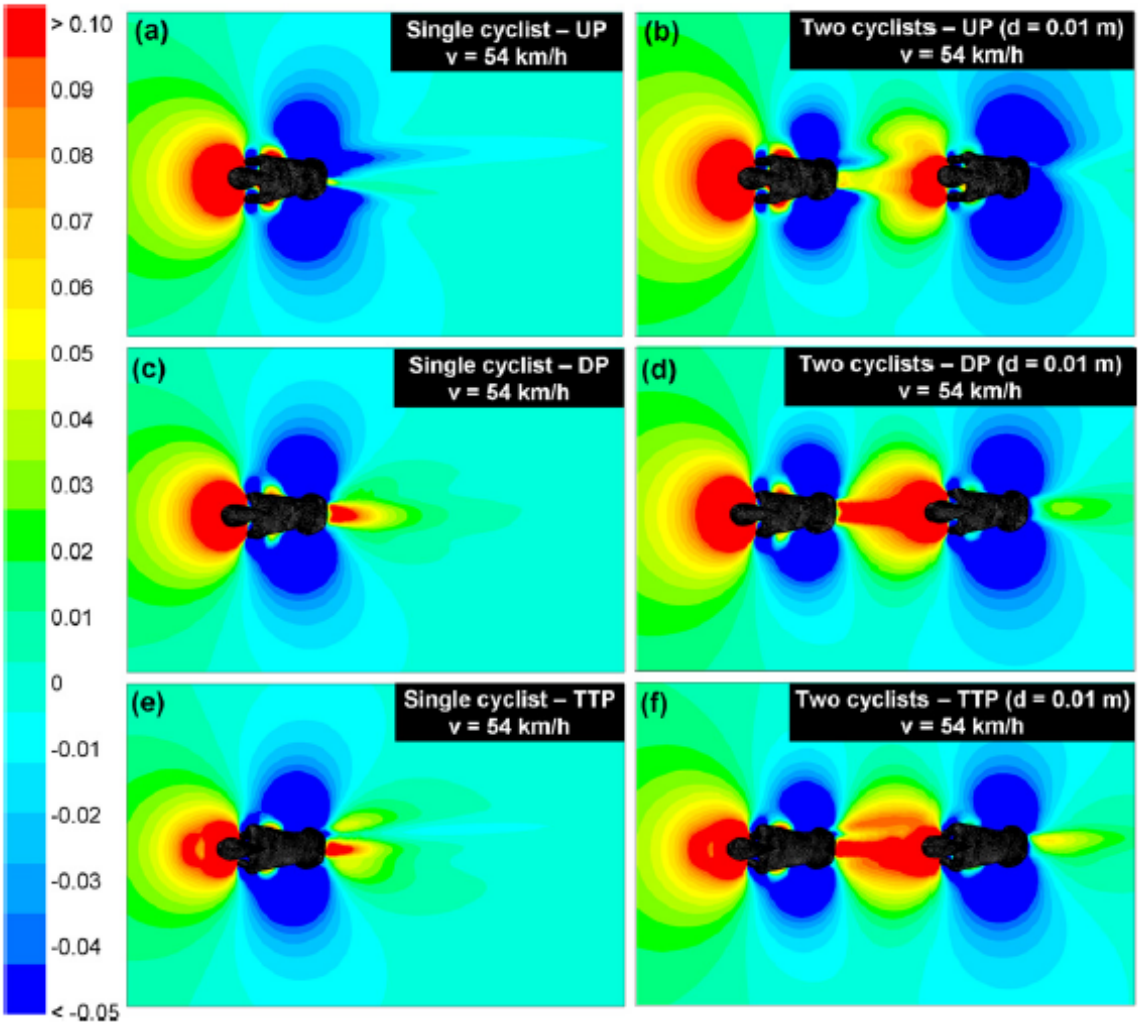

Figure 2.13: Pressure coefficients C_P in the horizontal plane at waist height for isolated cyclist (left) and two cyclists separated by $d = 0.01m$, at a speed of 54 km/h, from [10]

surements using cyclists in a brake-hood position [9]. It was found that even small changes in the yaw angle of the wind had an impact of the drag reduction of the trailing cyclist, but not so much on the lead cyclist. At an axial separation of 0.05 m, the drag reduction of the trailing cyclist was 47%, 40% and 30% for yaw angles of 0°, 3° and 5°.

The above mentioned studies on drafting are limited to wheel-to-wheel separation distances of less than 1m. Literature on whether there is an effect of a cyclist's wake on the drag reduction of a trailing cyclist at larger axial distances is limited. Brown et al. explores the development of the far-field wake and its effects on trailing riders using a cycling mannequin in the time trial position in a wind tunnel [11]. Observations of the wake development using dynamic pressure probes revealed that the asymmetry of the leg position produces an asymmetric wake. In the low drag positions of the legs (0° and 180°), the wake tends towards the side of the leg that is upstream, and in the high drag positions (90° and 270°), there is a large downwash towards the outstretched leg. Contour maps of the wake propagation can be found in figures 2,3

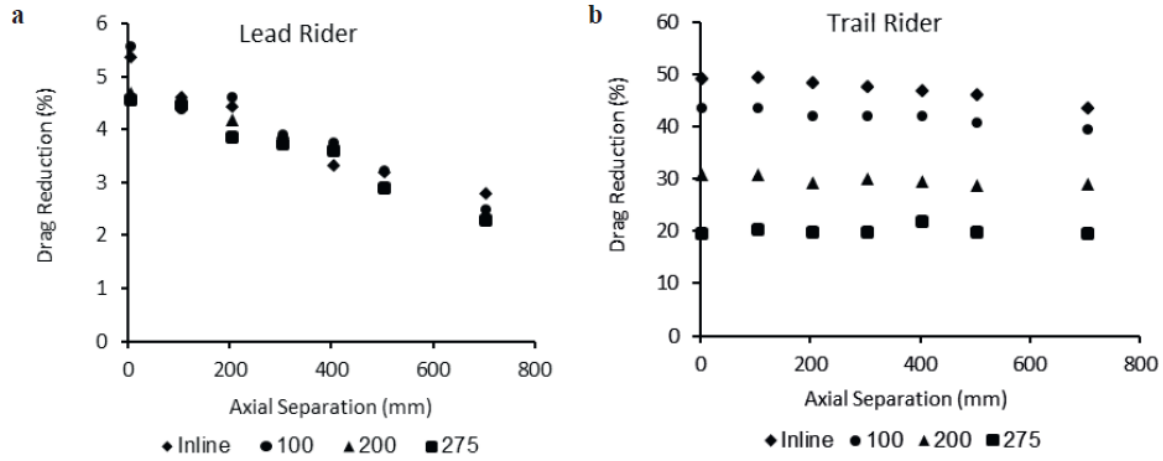

Figure 2.14: Percentage drag reduction for leading (left) and trailing (right) riders vs Axial separation at four different lateral distances from the centreline, from [6]

in [11]. Drag reduction estimates based on dynamic pressure loss were calculated for different axial separations, and these results are reproduced in figure 2.15. While not entirely accurate, these estimates provide a first step towards understanding the effects of riding in the far-wake of a cyclist.

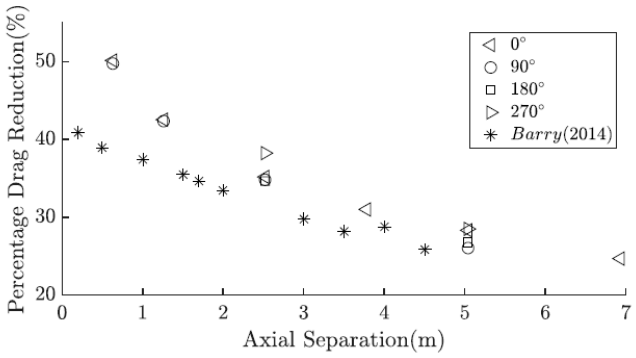

Figure 2.15: Percentage drag reduction for a trailing rider vs Axial separation for different leg positions: 0°, 90°, 180°, 270°, from [11]

2.3. Simulation of turbulence in a wind tunnel

To see the effects of the actual turbulent air stream on any wind tunnel tests, the turbulence levels measured in the velodrome can be simulated in a wind tunnel. Turbulent flows are complex and chaotic, and the best way to study such flows is by examining its most simple expression - homogeneous, isotropic turbulence [33]. Simulation of turbulence in a wind tunnel has evolved from simple passive grid-generated turbulence, to using active grids which push the limits of Re of the flow generated [36] [41]. This research will focus on the classic case of passive grids to generate turbulence, as it is sufficient for the range of Re that cycling falls under.

2.3.1. Grid generated turbulence

Grids and screens used in wind tunnels can serve to dampen or generate turbulence. A grid placed normal to a uniform upstream flow affects the flow in two ways which interact to produce a fairly homogeneous, isotropic flow downstream of the grid. The first, a manipulation effect, alters the spectrum of turbulence by changing the scale of upstream eddies according to the grid dimensions. The second is the wake effect which contributes to the energy of the downstream turbulent flow. This effect decreases the scale of the upstream eddies and is of relatively high frequency. The turbulence energy generated decays rapidly, with the eddies increasing in size with downstream distance [46]. The turbulence levels generated is a sum of the existing turbulence levels of the wind tunnel and the turbulence produced by the grids or screens.

The turbulence generated by a range of grids were examined via hot wire measurements by Roach [46]. The geometry of such grids can be defined using three parameters : the mesh length M, the wire/bar width d and the porosity β of the grid (figure 2.16). The porosity can be mathematically expressed as given in equation 2.10. It was found that the turbulence field generated is nearly isotropic at downstream distances greater than $\frac{x}{M} > 20 - 30$ (*x* refers to the streamwise distance measured from the location of the grid), and the length scales of the turbulent field are dependent on the rod/bar dimension. It was also concluded that grids made of round rods or wires were strongly influenced by the Reynolds number of the flow unlike the grids made of square bars or for perforated plates.

$$\beta = (1 - d/M)^2 \tag{2.10}$$

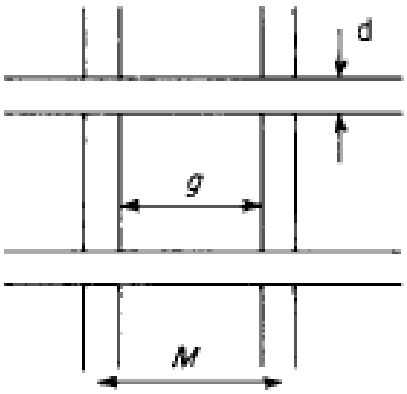

Figure 2.16: Geometry of a grid, from [46]

Investigations of Kurian et al. revealed that it is possible to control the length scales of the turbulence field generated while keeping the intensity of turbulence constant [33]. Note that to generate good quality turbulent fields, the mesh length *M* of the grid must be sufficiently small compared to the width of the wind tunnel. Turbulence generated using such methods is characterised by low Reynolds numbers [41].

2.3.2. Some applications of grid generated turbulence

There have been several studies on the simulation of atmospheric turbulence encountered by road vehicles in a wind tunnel. The aerodynamic performance of these vehicles depend on a number of factors, including the vehicle geometry and speed, air properties, wind speeds and direction, and the surrounding environment [39]. While it is near impossible to have repeatable terrestrial wind conditions, understanding the effects of mean turbulence levels that can be expected will provide better predictions of the drag experienced by the vehicles [61]. It is to be noted that there exists no specific set of ”rules” to follow when it comes to replicating a turbulence spectrum in a wind tunnel, it is mainly a trial and error based process.

A noteworthy example of turbulence simulation for road vehicles is the NRC Road Turbulence System (RTS) developed by McAuliffe et al. [38] for heavy-duty vehicles (HDV). They followed an eight step approach that involved measurement of on-road turbulence experienced by HDVs, testing four different passive turbulence-generating techniques on a small scale, and then extending a final concept based on these results to build a RTS. The final concept used obstacles in the settling chamber to generate large scale turbulent structures on the order of 1 m or more, with a turbulence intensity of 4% [38]. The same system was also used in the study of full-scale light-duty vehicles [39].

Watkins et al. replicated realistic turbulent environments to further the study of natural and man-made micro air vehicles (MAVs). In order to so, different screens and grids were used, along with changing the configuration of the test section itself to obtain larger scales of turbulence [62].

A study conducted by D’Áuteuil et al. on the measurement, simulation and effects of turbulence on the aerodynamic drag of a speed skater is perhaps the most relevant to this thesis [21]. The wind turbulence generated by a skater were measured in an indoor speed skating oval using a pressure probe. Through a trial and error process, the complete wind spectrum was replicated in a 2m $\times$ 3m wind tunnel using a combination of vertical flat plate obstacles in the settling chamber, to generate large scale vortices and increase the turbulence energy produced at lower frequencies, and a grid installed upstream of the model, to generate energy at higher frequencies. A schematic representation of this configuration is reproduced in figure 2.17a. The simulated turbulence, along with the mean and minimum turbulence levels measured in-situ is reproduced in figure 2.17b.

2.4. Discussion & Research Gap

The literature survey aimed to elaborate on the research available on the aerodynamic drag saving techniques currently available for cycling aerodynamics, particularly on the optimisation of skin-suits used by the cyclists, as well as the case of riding in the wake of another cyclist. While there have been massive developments over the past decades in these areas, two main gaps in the research have been identified and these will form the basis of this thesis.

The first of this is the fact that any wind tunnel tests of skin-suits, or cycling aerodynamics in general, are conducted in air streams that are designed to have very minimal turbulence levels. These flows in the wind tunnel are far from the true turbulent air flow conditions experienced by cyclists in indoor and outdoor events, which

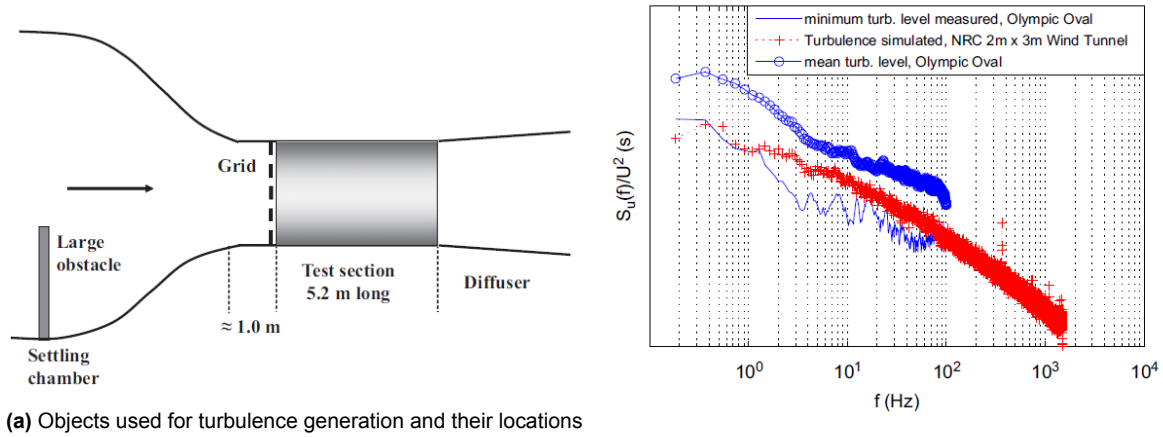

(a) Objects used for turbulence generation and their locations in a wind tunnel to replicate the measured turbulence in speed skating, from [21]

(b) Normalised longitudinal power spectral densities of the flow, from [21]

Figure 2.17: Turbulence simulation in a wind tunnel for speed skating [21]

means that any drag results obtained from these tests are not truly accurate to what the cyclist experiences on track. The second point to be considered is that while the effects of riding in the near-wake of another cyclist have been investigated quite thoroughly, there exists minimal literature on whether the far-wake of a leading cyclist has an effect on the trailing cyclist. Cycling events such as the individual pursuit involve two cyclists starting the race at diametrically opposite locations, and it is worthwhile to study if there are potentially any effects of the far-wake of a cyclist on the drag of the trailing rider.

The study on speed skating conducted by D'Auteil et al. offers some similarity to the first point and it was found that including the turbulence levels measured on an ice skating rink have an effect of the measured drag forces [21]. Since speed skaters and cyclists operate in similar Reynolds number regimes, it is expected that similar results will be obtained for cyclists as well. The effect of far wakes were discussed by Brown et al. and it is seen that far-wakes do have an effect on the drag of the cyclist.

2.5. Research Questions & Outline

A review of the latest advancements in optimising the aerodynamics of cyclists has been presented in the previous sections, along with the identification of gaps in the research. Based on the outlined considerations, the research questions that define this thesis work can be formulated :

”What are the effects of the turbulence levels measured in an indoor velodrome on the aerodynamic drag of a cyclist ?”

1. What turbulence intensities and spectra are encountered by a cyclist in an indoor velodrome?
    (a) In the presence of an individual rider, at varying rider speeds?
    (b) When riding in the far wake of a lead rider, at different distances of separation?
2. How can these measured turbulence levels be replicated in a wind tunnel?
    (a) Can the turbulence intensities be simulated accurately using passive turbulence generation techniques?
    (b) To what extent can the generated turbulence spectrum be matched to the results obtained from on track measurements?
3. What are the effects of this turbulence on the drag crisis of a circular cylinder?
    (a) In the case of a smooth surfaced cylinder?
    (b) In the case of a rough surfaced cylinder?

The first sub-question is directed towards the measurement of real time flow conditions experienced by a cyclist in a velodrome. The second and third sub-questions address the impact of the simulated free stream turbulence on the current methods of testing skin-suits in a wind tunnel by means of direct drag force measurements.

3

Methodologies

3.1. Three-hole Pressure probes

Three-hole pressure probes are intrusive measurement devices that provide the local value of flow velocity and direction in two dimensions. The principle behind these devices is that the static pressure distribution over the surface of a solid body inserted in a flow varies from a maximum at its stagnation point to values lower than the static pressure in the free-stream [51]. For a bluff body, this maximum pressure is equal to the total pressure and can be mathematically expressed by the Bernoulli's principle given in equation 3.1.

$$p_{tot} = p + \frac{\rho U^2}{2} \tag{3.1}$$

where p_{tot} represents the total pressure, which is the sum of the static pressure p and the dynamic pressure $\frac{\rho U^2}{2}$. The Bernoulli's principle is valid for incompressible, inviscid and steady flows. It is valid everywhere in the flow if the flow is irrotational, or in the case of rotational flows, along a streamline. In an incompressible flow, the total pressure at any point on the bluff body can be related to the total pressure of the fluid far upstream, and the above equation can be modified as given in equation 3.2 [5].

$$p + \frac{\rho U^2}{2} = p_\infty + \frac{\rho U_\infty^2}{2} \tag{3.2}$$

where p and U are the static pressure and flow velocity at any point on the surface of the body.

The static pressure taps of a pressure probe are arranged at the tip of the probe, where the flow is least affected by the presence of the probe itself. While a variety of geometries of these probe tips have been used before [51], in this research, the focus is on the hemispherical probe tip. To derive a numerical relation which connects the pressure measured at the probe tips to the local flow velocity, a potential flow solution can be used due to the simple contour of the probe tip geometry. For a hemisphere, the velocity at any point on the surface is given by equation 3.3 [5].

$$U_\theta = \frac{3}{2} U_\infty \sin(\theta) \tag{3.3}$$

where θ is the angular distance of the point of interest from the stagnation point of the contour and U_θ denotes the velocity magnitude at that point. Substituting this relation in equation 3.2 for the location of each of the three pressure taps results in the following set of equations.

$$\begin{aligned} p_0 &= p_{tot} - \frac{9}{8}\rho U_\infty^2 \sin^2(\alpha) \\ p_1 &= p_{tot} - \frac{9}{8}\rho U_\infty^2 \sin^2(\alpha - \theta) \\ p_2 &= p_{tot} - \frac{9}{8}\rho U_\infty^2 \sin^2(\alpha + \theta) \end{aligned} \tag{3.4}$$

An illustration of the hemispherical probe head is shown in figure 3.2 to visualise the variables in the set of equations given in 3.4. The pressure ports are denoted by 0, 1, 2 and are separated by an angle of θ. The measured pressures are p_0, p_1, p_2 respectively, with the total pressure p_{tot}, magnitude of flow velocity U_∞ and flow direction α being the unknowns calculated using these equations.

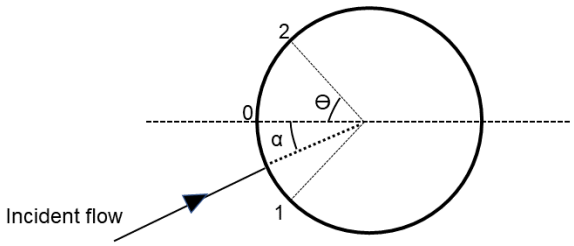

Figure 3.1: A sketch of the hemispherical probe head

In addition to this theoretical analysis, it is also necessary to calibrate the probe using experimental techniques, to account for any machining errors with the location of the pressure taps on the tip of the probe. Calibration of such probes are carried out in an open jet wind tunnel to eliminate the effects of blockage that come with a closed test section. The probe is placed at the exit and in the centre of the test section, and is carefully aligned with the flow direction so that the probe is nearly parallel to the flow. The free-stream velocity is controlled using the wind tunnel system and measurements are carried out at varying flow speeds. A calibration coefficient can then be determined using the wind tunnel velocity and the velocity measured by the probe itself [40] [14].

While several advanced flow measurement techniques have been developed over the years, the three-hole pressure probe is the chosen measurement technique in this research for the following reasons. These probes are more robust than hot-wire anemometers, which makes them suitable for conducting field measurements. They are also less susceptible to particulates in the flow. When compared to Laser-Doppler Velocimetry (LDV) and Particle-Image Velocimetry (PIV), multi-hole pressure probes are not limited by the requirement of optical access to the point of measurement. Since the aim is to measure the turbulence velocity fluctuations over the course of the bicycle track, LDV and PIV are unsuitable due to the limited measurement area that they cover.

3.2. Hot-wire anemometry

Hot-wire anemometry is an established technique used for point-by-point measurement of fluid velocities. The hot-wire sensor, which is an electrically conductive wire, is heated by the passage of an electric current via the Joule effect and subsequently cooled by the incident flow due to convective heat transfer. The rate of cooling is directly proportional to the temperature change of the wire, and in turn, the flow velocity [18]. Hot-wire sensors are typically made of platinum or tungsten, and have small dimensions (0.5-5μm diameter, 0.1-1 mm length). These small dimensions of the wire lead to improved spatial resolution and reduced thermal inertia, which also leads to optimal frequency response or temporal resolution.

The electronic circuit of the hot-wire system is primarily made up of a Wheatstone bridge. A Wheatstone bridge consists of four arms containing a resistor each, one of which is the hot-wire itself. The bridge is said to be *balanced* when the ratio of resistances R and R1 is equal to that of R2 and R3. While the bridge can be operated in different modes, the Constant Temperature Anemometer (CTA) is commonly accepted as the standard configuration and hence will be used in this thesis. The basic principle behind the CTA is that the wire temperature is kept constant in time. This eliminates the risk of probe burnout and increases the frequency response to 10-100 kHz. In order to achieve this, CTA employs a feed-back circuit in addition to the Wheatstone bridge. When the hot-wire is placed in a flow, forced convection causes the temperature of the wire to drop. This temperature is linearly related to the resistance of the probe, and hence leads to a drop in resistance of the wire, disrupting the balance of the bridge. The feedback control senses this change and acts to increase the current flowing through the circuit, thus keeping the temperature constant and restoring the balance of the bridge.

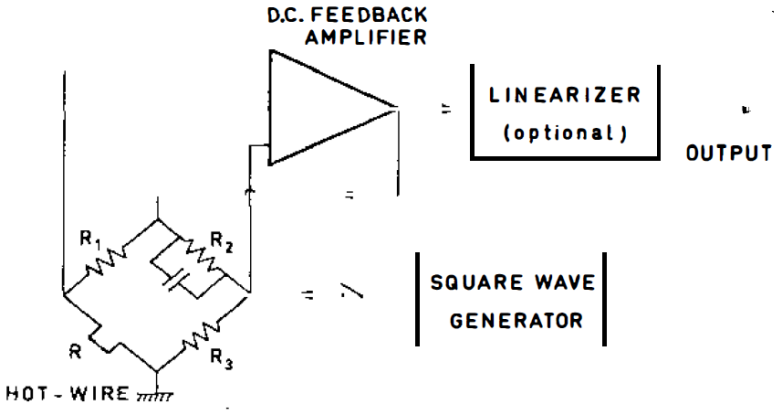

Figure 3.2: CTA circuit [18]

The feedback signal is representative of the changes in the flow variables [18]. In order to obtain a mathematical representation of this, a simplified static analysis can be employed. When the bridge is balanced, the hot-wire is in thermal equilibrium, with negligible heat loss due to conduction and radiation. This implies that the Joule heating *W* equals the convective heat transfer *H*.

$$I_w^2 R_w = h_f A_w \left(T_w - T_f\right) \tag{3.5}$$

where I_w represents the current flowing through the wire, R_w represents wire resistance and T_w is the wire temperature. The temperature of the fluid is represented by T_f and the convective heat transfer coefficient by h_f. Replacing h_f by the Nusselt number Nu gives equation 3.6, where the Nusselt number is the ratio of convective to conductive heat transfer coefficients.

$$I_w^2 R_w = (Nuk_f/d_w)\, A_w\, (T_w - T_f) \tag{3.6}$$

The equation above can be further manipulated by making use of the relation between Nusselt number and the Reynolds number in the forced convection regime to obtain the following relation 3.7 between the voltage drop across the wire E_w and the flow velocity U.

$$I_w^2 R_w^2 = E_w^2 = (T_w - T_f)\,(A + BU^n) \tag{3.7}$$

The non-linear response of the hot-wire sensor can be mathematically expressed as $E^2 = A + BU^n$, where A,B,n are constants representative of the system and are obtained from an experimental calibration procedure. This involves measurement of flow velocity using a standard instrument, such as a Pitot tube, and the corresponding voltage using the hot-wire itself for several flow conditions. Using this set of data points, the calibration constants can be determined via a non-linear curve fit. It is necessary to perform this calibration procedure at several occasions during testing, to account for variations in the ambient temperature. A typical static calibration curve is presented in figure 3.3.

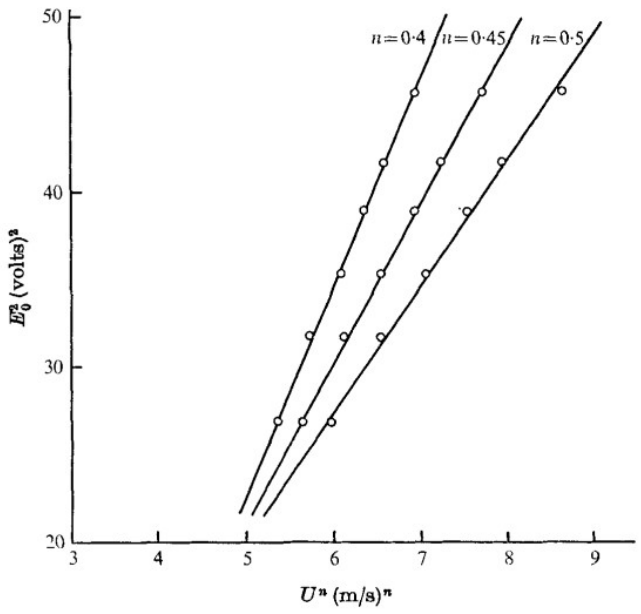

Figure 3.3: Static calibration of CTA. n = 0.5 is the value for the conventional King's law calibration. Alternative forms of static calibration lead to other values of n, details of which can be found in [44]

3.3. Force Balance

Force balances are devices that are designed to measure some or all of the aerodynamic loads experienced by a model in a wind tunnel flow. These force balances can be broadly categorised into internal and external type balances, based on their position relative to the model to be tested. They can also be categorised based on the measurement principle followed, as mechanical balances, strain gauge balances, piezoelectric balances and magnetic suspension balances [26]. A complete survey of the different categories of force balances is beyond the scope of this thesis (see [26] for an overview).

The most commonly used amongst these is the strain gauge balance. When such a balance experiences a load, the flexures in the balance deflect. The deflections are measured by a strain gauge which produces a change in electrical resistance when its length changes. These individual strain gauges are wired to a Wheatstone bridge to measure the changes in resistance as a voltage signal [4][26]. An example of such a balance can be found in Hoffman et. al. (figure 2) [30]. This research utilises an external strain gauge balance to measure the six components of aerodynamic forces and moments on automobile shapes.

Huang et. al. designed and constructed a force balance to measure the thrust and the lateral force experienced by a Vertical axis wind turbine (VAWT) using S-shaped load cells. These load cells are connected using flexural rods to ensure that they measure only tensile or compressive forces. They are mounted on a stiff standing frame capable of avoiding vibrations and deformations [31]. A schematic of this balance and their model is shown in figure 3.4. The same balance will be used in this research to measure the drag force experienced by a circular cylinder in a turbulent air stream.

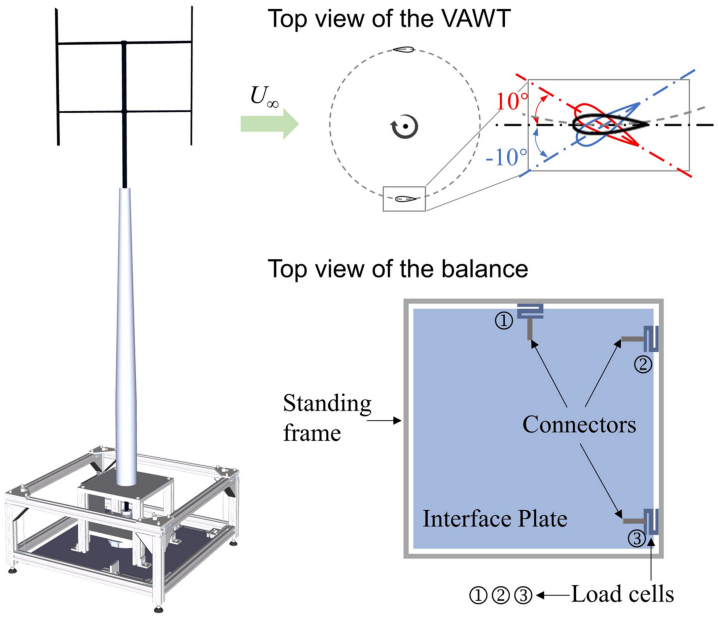

Figure 3.4: A schematic of the force balance designed by Huang et. el. and the model used [31]

Crouch et. al. measured the drag force experienced by a cycling mannequin around a complete crank cycle. To do so, a six component piezoelectric type force balance was utilised [20]. These type of balances work on the principle of the ”piezo-

electric effect", wherein the material produces an electric charge when it is exposed to mechanical stress [26]. The balance consisted of four individual three-component piezoelectric force transducers positioned in a horizontal quadratic arrangement to measure the force and moment coefficients [20].

4

Velodrome Set up and Procedures

4.1. Velodrome and model details

4.1.1. The Velodrome

Track cycling events are typically conducted on a velodrome track, which is an oval track designed based on the rules and regulations provided by the UCI [60]. For the purpose of this research, an indoor Velodrome is chosen due to the controlled environment that it offers, which is beneficial when trying to determine the turbulence caused due to the presence of cyclists exclusively. A scheme of a typical velodrome track is shown in figure 4.1. All the field measurements in this thesis are conducted in The Omnisport Velodrome in Apeldoorn, the Netherlands. This track is 250m long and 7m wide (figure 4.1). The measured ambient pressure, temperature and air density on the track on the day of testing is 1.02×10^5 Pa, 26.28°C and 1.18 kg/m^3 respectively.

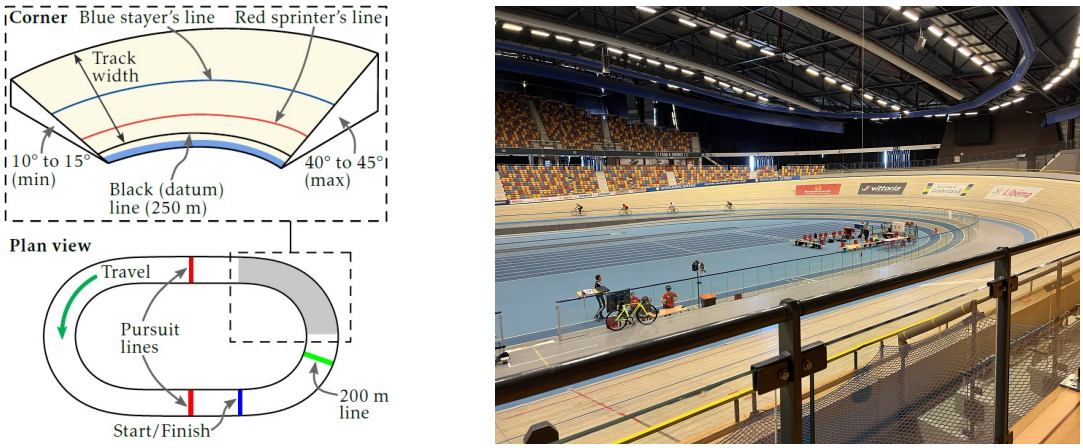

Figure 4.1: A cross-section of a typical velodrome track [27] (left) and the Omnisport Velodrome in Apeldoorn (right)

4.1.2. The instrumented bicycle

Testing is done with a Scott Plasma 5 Time Trial bicycle shown in figure 4.2. It has a Shimano Dura Ace powermeter. It is also equipped with a Garmin speed sensor, fixed

to the hub of the rear wheel, and a Garmin cadence sensor which is fixed to the crank arm. Both these sensors sample the wheel speed and cadence data at a frequency of 1 Hz. A Garmin Edge 130 Plus bike computer is fixed to the handlebar of the bicycle and is used to acquire the powermeter, speed and cadence data.

Figure 4.2: The bike used in the velodrome experiments

Turbulence data is collected using the three-hole pressure probes from AeroLab Tech, Canada. The probe is fixed to the Aero Bars of the bicycle using a sensor mount specifically designed for this purpose (figure 4.3). Two different models of these sensors are used during this research. The first is a sensor custom-made for the purpose of this thesis, with a sampling frequency of 1000 Hz. This sensor consists of two differential pressure transducers, each connected to the central hole of the probe via one port and to the left or right angled holes of the probe via the other port. These pressure transducers are 0.5" H_2O miniature amplified output pressure sensor. The sensor collects data in the form of instantaneous differential pressures and stores them on a micro SD card, from which the required turbulence data can be calculated. The second kind of sensor used is the commercially available AeroPro sensor, modified to collect data at 40 Hz instead of their standard 20 Hz set-up. This sensor has three differential pressure transducers, with one of the ports connected to each of the three holes of the probe, and the second port connected internally. It is also equipped to collect a variety of other data, for example the ambient temperature, pressure, density and accelerometer data, in addition to the differential pressures. The rides can be controlled via AeroLab's own iOS application called "AeroLink" and it has multiple test protocols available for testing [3].

Two professional male riders, both in the range of 170-180 cm height, 65-75 kg weight, are employed to take part in this study. The primary rider is on the instrumented bike through the duration of the measurements. This work has been approved by the ethical committee of TU Delft and the riders have signed the informed consent.

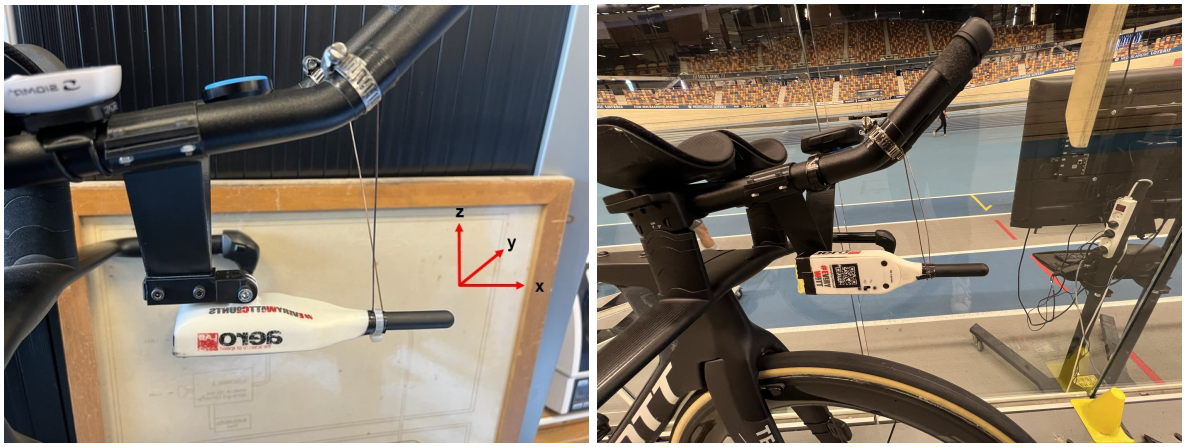

(a) Sensor mounted in the x-y configuration **(b)** Sensor mounted in the x-z configuration

Figure 4.3: Sensor configurations

4.2. Experimental procedure

A layout of the velodrome track with the start and end positions, as well as the co-ordinate system used in these measurements are provided in figures 4.1 and 4.4 respectively. Every run of the measurement campaign follows the same layout : two laps around the track for the rider(s) to get to the required measurement speed, and five laps over which the turbulent flow data was collected. The tests are performed twice for each configuration for the sake of repeatability. Since a three-hole pressure probe only allows for calculations of velocity fluctuations in two dimensions, the probe is rotated by 90° around its axis so as to get the complete picture of the flow-field in three dimensions. These probe configurations are depicted in figure 4.3. The arduino-based sensor is employed for the calibration tests and the turbulence measurements while the AeroPro sensor is used to collect additional data towards the end of this experiment.

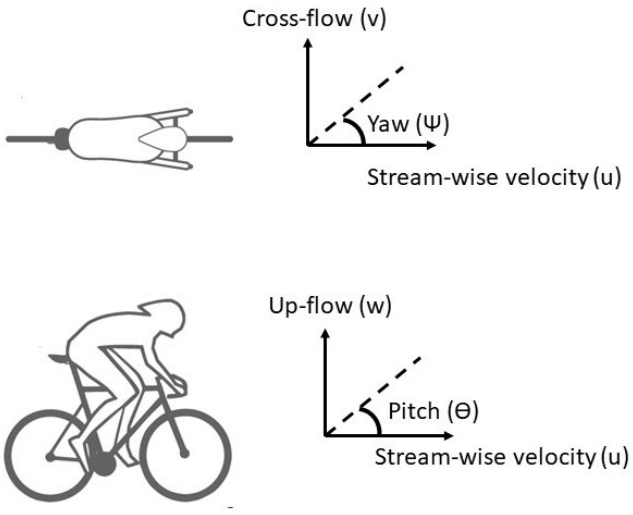

Figure 4.4: The three components of velocity u, v, w and yaw (ψ) and pitch (θ) angles

The first step of the campaign is to determine the calibration factor that corrects for the influence of the rider on the pressure field in the front of the bicycle. This allows for calculations of the true velocity fluctuations in the air caused by a cyclist. Assuming a linear relationship between the measured and true pressures, the tests are conducted in the following way. The cyclist on the instrumented bicycle is asked to ride at three different speeds of 35 km/h, 45 km/h and 55 km/h in a randomised order, to account for any drifts in the measurements. The configuration of the sensor is then changed and the process in repeated. This experimental procedure is tabulated in table 4.1. The data collected at both configurations of the sensor is collectively used to determine the linear calibration coefficients used to determine the true air speed in front of the cyclist, and is given in figure 4.5.

Run	Rider Speed (km/h)	Time (s)	$\Delta P_{0,1}$ (Pa)	$\Delta P_{0,2}$ (Pa)
1	35	-	-	-
2	45	-	-	-
3	55	-	-	-

Table 4.1: Test matrix for the calibration of the sensor followed for both configurations of the sensor individually

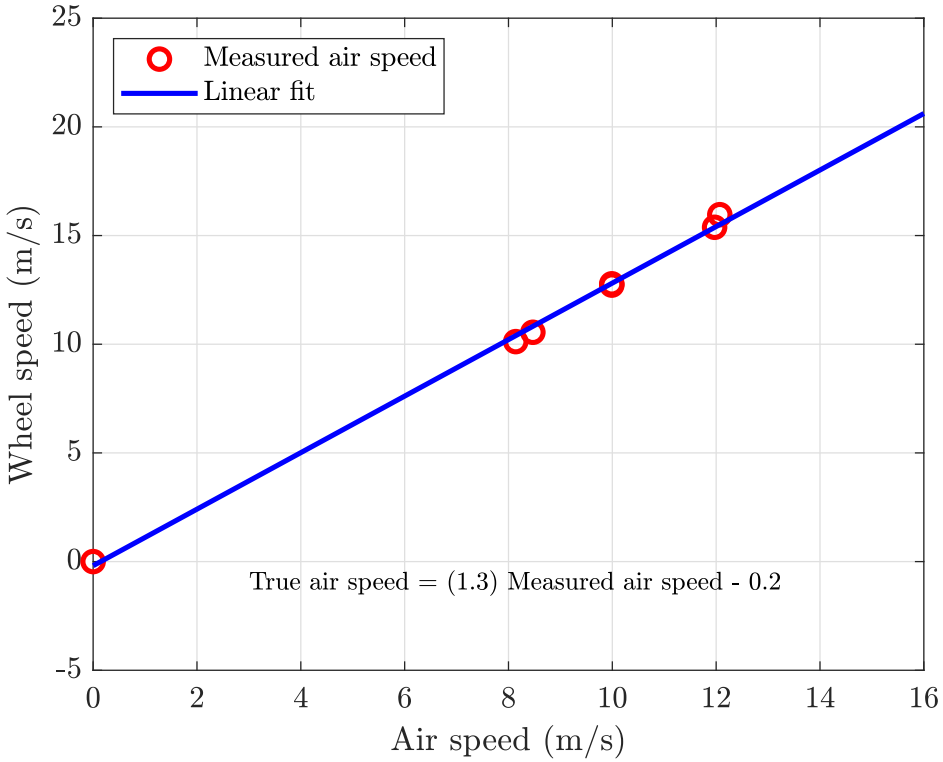

Figure 4.5: Probe calibration to account for the influence of the cyclist on the pressure field in front of the bicycle

For the remaining tests, the speed at which measurements are conducted is fixed

at 45 km/h. To gather the data of turbulence levels generated due to the presence of a single cyclist on track, the cyclist on the instrumented bike performed tests at the required speed for both configurations of the sensor. The next step of the experimental campaign involves measurements using two cyclists. The variable in this case is the separation distance between the two riders. To quantify the effects of ”far wake” on a cyclist, three different separation distances are tested : half a lap, quarter of a lap and one eighth of a lap. Since the distances in consideration are large, they are measured and maintained using a combination of the markings on track and visual inspection by the people observing the experiment. These measurements are repeated for both configurations of the sensor at all different distances, and are summarised in table 4.2. Finally, two runs are made with just the single cyclist on track using the AeroPro sensor in both sensor configurations, to quantify the vibrations of the sensor mount on the velodrome track.

Run	Separation distance (m)	Time (s)	$\Delta P_{0,1}$ (Pa)	$\Delta P_{0,2}$ (Pa)
1	Isolated rider	-	-	-
2	$\frac{1}{2}$ lap	-	-	-
3	$\frac{1}{4}$ lap	-	-	-
4	$\frac{1}{8}$ lap	-	-	-

Table 4.2: A condensed form of the test matrix followed to measure turbulence levels in the velodrome. All runs are conducted at a rider speed of 45 km/h

4.3. Data processing

4.3.1. Components of flow velocity and flow direction

The probe used for collecting turbulence data, that is the arduino-based sensor, outputs two differential pressures at a frequency of 1000 Hz. The flow velocity components and the flow direction can be calculated by modifying the mathematical relations obtained from Bernoulli’s principle and potential flow theory expressed in equations 3.4. Considering how the pressure transducers are connected within the sensor, described in section 3.1.2, these equations can be modified to the following form:

$$\begin{aligned} \Delta P_{0,1} &= p_{tot} - \frac{9}{8}\rho U_\infty^2 \left(\sin^2(\alpha) - \sin^2(\alpha - \theta)\right) \\ \Delta P_{0,2} &= p_{tot} - \frac{9}{8}\rho U_\infty^2 \left(\sin^2(\alpha) - \sin^2(\alpha + \theta)\right) \end{aligned} \tag{4.1}$$

where $\Delta P_{0,1}$, and $\Delta P_{0,2}$ refer to the differential pressures measured between port 0,1 and port 0,2 respectively. Since the angle θ is known to be 45°, this results in two equations and two variables that can be solved on MATLAB.

Once the velocity magnitude and flow direction is obtained, the velocity components can be calculated as follows:

$$u = U_\infty \cos(\alpha) \quad v = U_\infty \sin(\alpha) \tag{4.2}$$

It is to be noted that the above equations are expressed for the x-y configuration of the probe. Therefore, u represents the stream-wise velocity component, v represents the lateral velocity component and α is the yaw angle. A similar procedure is followed for the x-z configuration, which results in w, the vertical velocity component and ψ, the pitch angle.

4.3.2. Turbulence statistics

The velocities obtained from the pressure probe data can be decomposed into its mean flow $\overline{U}$ and its fluctuating component $U^{'}$ as given in equation 4.3. This is commonly known as Reynolds decomposition [45].

$$U = \overline{U} + U^{'} \tag{4.3}$$

The characterisation of turbulent flow fields by its intensity, energy spectrum and length scales was discussed previously in section 2.1.2. Once the measured velocity is decomposed into a mean and fluctuating component as in equation 4.3, the turbulence intensity can be calculated using equation 2.4. The power spectral density (PSD) of the velocity fluctuations is estimated using Welch's method [63]. In this method, the time signal is split into a finite number of overlapping segments. A Hamming window is employed as the windowing function [32], which mainly reduces the truncation effects at the edges of the segments. Windowing results in a loss in signal power, which is compensated for by the overlapping segments, with the overlap set to 50% of the segment length. A Discrete Fourier Transform (DFT) is then carried out, and the output is squared and then averaged over all the segments to obtain the PSD estimate [32].

The integral length scale of turbulence, defined by equation 2.7, is estimated using the exponential method, which is based on the correlated turbulence structures [55]. In this method, it is assumed that Taylor's frozen turbulence hypothesis holds. The auto time correlation coefficient ρ_τ is first calculated as follows [52]:

$$\frac{\overline{u(t)u\,(t')}}{\overline{u^2}} \equiv \rho(\tau) \tag{4.4}$$

This coefficient is then integrated over the time domain up to the region where ρ_τ first falls to the value $\frac{1}{e}$. The resulting value that is obtained represents the integral time scale, from which the integral length scale is estimated by simply multiplying the value with the mean velocity [55].

5

Wind tunnel Set up and Procedures

5.1. Wind tunnel Facility and experimental set-up

5.1.1. The W-Tunnel

Wind tunnel measurements are conducted in the W-Tunnel, an open-loop, open-jet wind tunnel situated at the High Speed Laboratory of TU Delft. This tunnel operates in the subsonic regime, with a maximum achievable flow velocity of 35 m/s [56]. The flow can be controlled by setting the revolutions-per-minute of the centrifugal fan, which is driven by a 16.5 kW electric motor. This centrifugal fan drives the flow into the plenum of dimensions 2.0 m $\times$ 1.5 m $\times$ 2.0 m. The flow then passes through a diffuser into the settling chamber. The settling chamber contains two gauzes to reduce the turbulence intensity of the flow, keeping it at a minimum of 0.5 %. While replicating a certain turbulence level in a wind tunnel, the resulting turbulence that is obtained is a combination of the existing tunnel turbulence and the turbulence generated through the specific method employed [46], which makes the low turbulence of the tunnel an important parameter for this thesis. The flow is then accelerated through a contraction, nozzle and exits through a square test section of length 0.8 m and a cross-section of 0.4 m $\times$ 0.4 m [57].

Figure 5.1: The contraction and test section (left) and the external ventilation system of the W-Tunnel, reproduced from [57]

5.1.2. Turbulence generation

Grids placed normal to a uniform flow in a wind tunnel is the simplest, and most convenient method of turbulence generation. In order to replicate a specific wind spectrum, a trial-and-error based approach is followed to select the right configuration of grids that will generate the required turbulence spectrum and turbulence intensity. Additionally, if a complete wind spectrum needs to be replicated in a wind tunnel, that is, the precise amount of energy at both low and high frequencies, a combination of grids and large obstacles needs to be considered and tested.

In this research, four different grids, depicted in figure 5.2, are utilised to determine the best fit for the target spectrum to be achieved. Grid 1 is a square mesh made up of rectangular bars, Grid 2 a perforated plate, and Grids 3 and 4 are square meshes made up of thin, cylindrical wires. Grid geometry can be defined by three parameters: the bar width and hole/cylinder diameter "d" (based on the type of grid), the mesh width "M", and the porosity "β", as discussed in section 2.3.1. The dimensions of these four grids can be found in table 5.1. The grids were individually fixed to the inlet of the test section as shown in figure 5.3.

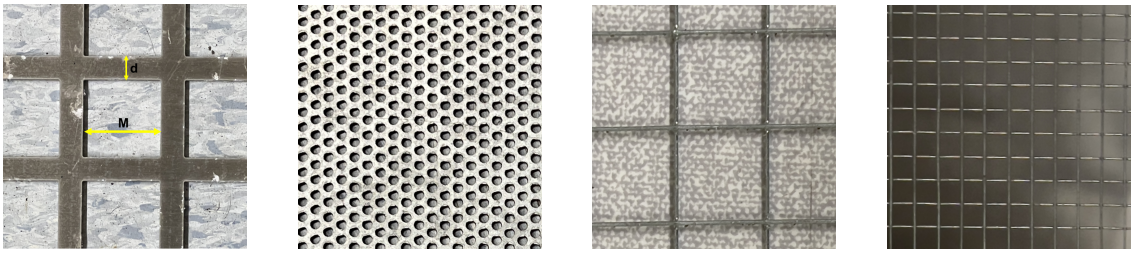

(a) Grid 1 **(b)** Grid 2 **(c)** Grid 3 **(d)** Grid 4

Figure 5.2: Different grids investigated

Grid	d (mm)	M (mm)	β
Grid 1	10	40	0.56
Grid 2	2	5	0.12
Grid 3	0.65	12.7	0.90
Grid 4	0.65	6.35	0.80

Table 5.1: Geometric parameters of the Grids

For the large obstacles required to generate turbulence energy at lower frequencies, square cylinders of different dimensions are fixed in the settling chamber of the wind tunnel and tested. Through this process, a combination of two square beams fixed beside each other is found to be the best fit. This set-up results in a rectangular cross-section of 0.095 m $\times$ 0.190 m.

5.1.3. Cylinder model

To quantify the effects of the turbulence generated on the aerodynamic drag, a simplified cylinder model representative of a cyclist limb is used. This circular cylinder had a diameter of 0.08 m and a height of 0.6 m. To simulate a smooth and rough surface on

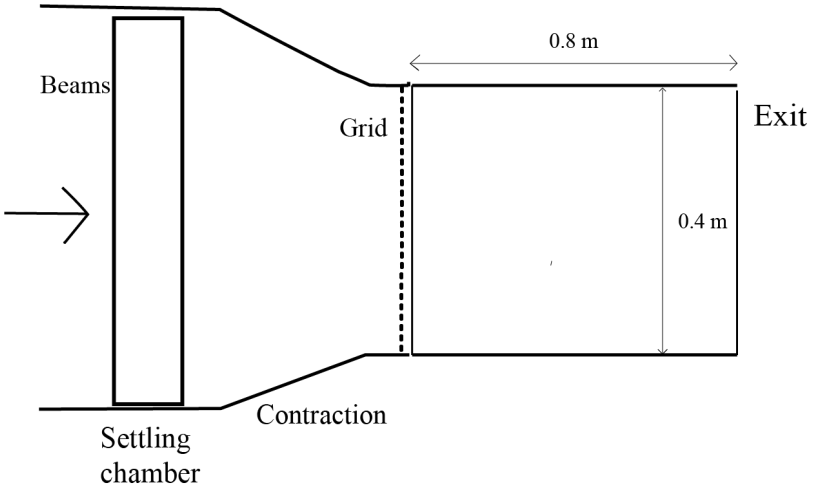

Figure 5.3: Side view of the experimental set-up

the cylinder for the different drag measurements, two different fabrics are fitted over the cylinder. These are depicted in figure 5.4. The ”smooth” blue fabric is made up of lycra and the ”rough” white fabric is manufactured by Eschler Textil (product code : 63858).

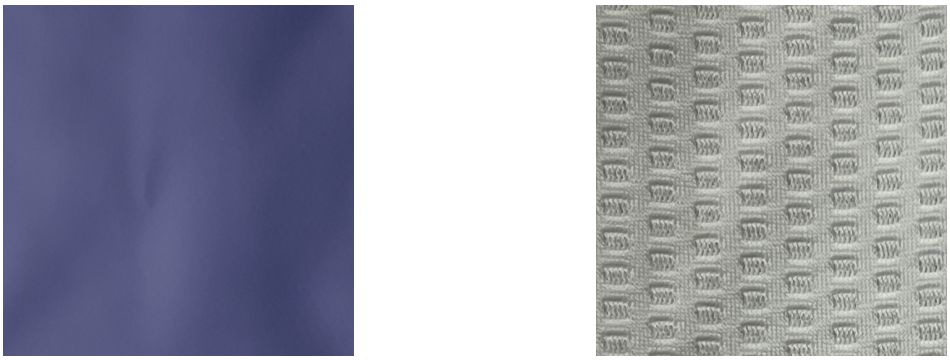

(a) Smooth fabric **(b)** Rough fabric

Figure 5.4: Fabrics used over the cylinder model

5.2. Simulation of wind turbulence

Turbulence generated in the wind tunnel was measured by the arduino-based sensor used in the velodrome. This sensor is fixed right at the exit of the test section, as shown in figure 5.5a and this position was maintained for all measurements. This gives the details of the flow turbulence that is encountered by the cylinder which is placed in the same location for drag measurements. The turbulence generated in the W-tunnel in its standard configuration is first measured, and this serves as a baseline for all other turbulence measurements. The four grids and the obstacle and the settling chamber are tested individually, as well as in combination, to find the best fit to the turbulence levels measured in the velodrome. For every test configuration, measurements are taken at 10 m/s and 15 m/s. These flow velocities are chosen because

they correspond to the typical cyclist speeds in a velodrome. With the measured data, the flow velocities and the turbulence statistics are evaluated as explained in section 4.3.

(a) Measurement of simulated turbulence

(b) Balance measurements of a rough cylinder

Figure 5.5: Wind tunnel experimental set up for turbulence measurements (left) and drag force measurements (right)

5.3. Pressure probe vs HWA

In order to gain a better understanding of the pressure probe and its limitations, the flow turbulence measured using the probe and a hot-wire anemometer are compared to each other. This is done so for two test cases - the wind tunnel as is and turbulence generated by Grid 1. The hot-wire sensor used is a Dantec Dynamics 55P11, a 5μm platinum plated tungsten wire directly welded to the prongs. This probe allows for measurement of the flow velocity in one dimension. The system is operated using a DANTEC 56C17 CTA bridge and the raw voltage data is acquired using a National Instruments BNC-2110 block connector connected to a NI PCI-6024E data acquisition board. LABVIEW software is used to read and store this data. This measured voltage is converted to flow velocity magnitude through a calibration process. The hot-wire is fixed at the same location as the sensor, the exit of the test section, and measurements are conducted at a sampling rate of 10 kHz, for duration of 30s.

The overheat ratio is set to 0.5 and calibration is performed once at the start of the measurement campaign. The hot-wire sensor is placed horizontally in the free-stream, and measurements are conducted at different flow speeds. The flow velocity is separately measured by the differential pressure system in the W-Tunnel. The voltage and the velocity measured can be used to derive a fourth-order polynomial relationship, based on King's law given in equation 3.7. These calibration measurements are

sampled at a frequency of 2 kHz for a duration of 5s. Figure 5.6 shows the calibration curve obtained from this procedure, and the King's law coefficients derived from it.

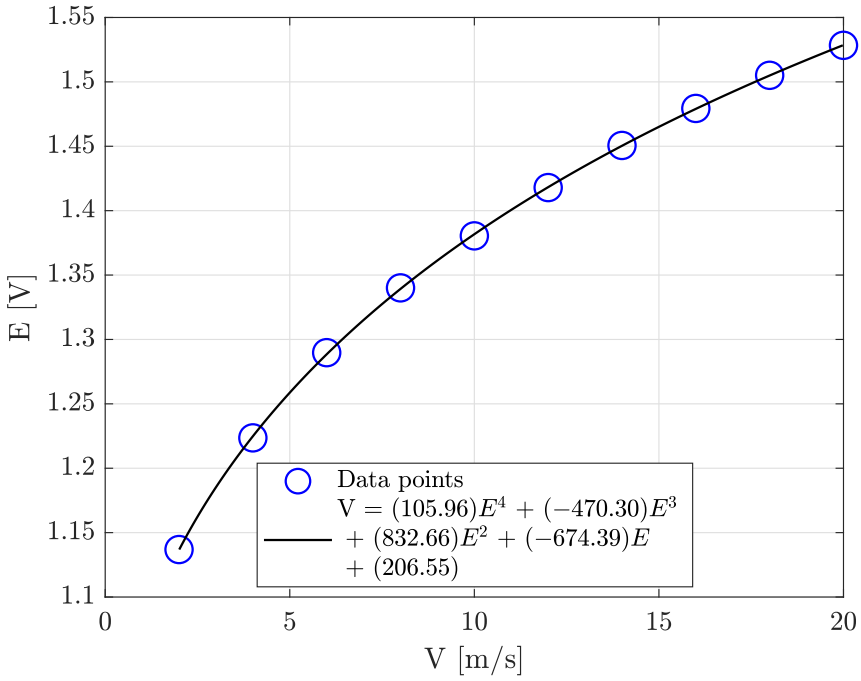

Figure 5.6: Hot-wire calibration

The turbulence spectra obtained from the pressure probe and hot-wire measurements for a flow through the wind tunnel in the absence of turbulence generating mechanisms are shown in figure 5.7. The tests were conducted at two different flow speeds - 10 m/s and 15 m/s. The measured spectral content below a frequency of 10 Hz using the probe and the hot-wire are quite similar at both wind tunnel speeds. Beyond 10 Hz, the sensor does not seem to pick up the high frequency, very low amplitude signals. This is attributed to the fact that the pressure sensor has a higher noise floor than the hot-wire sensor.

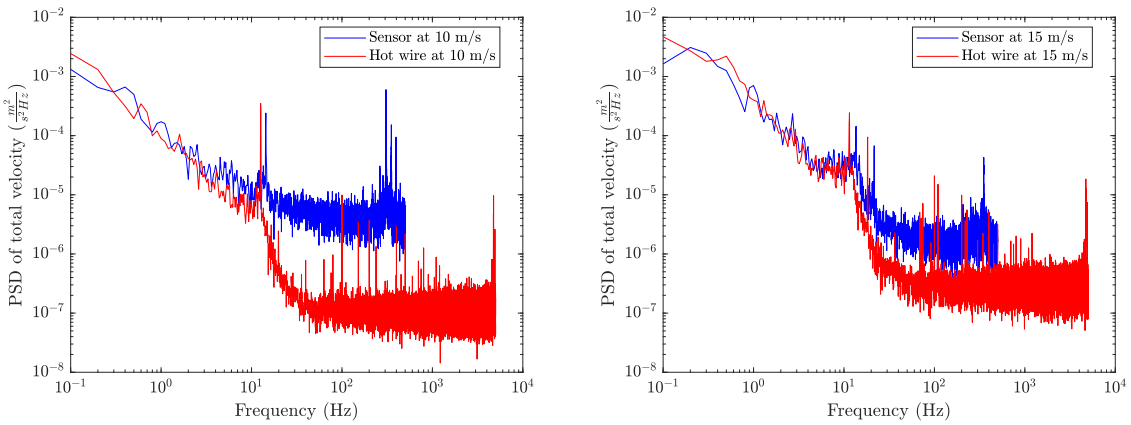

Figure 5.7: PSD of total velocity from probe and hot-wire measurements for the wind tunnel configuration with no turbulence generating mechanisms

The measured spectra are much closer in agreement in the case of a turbulent flow generated by grid 1, at both flow speeds tested. This is because the energy of turbulent flow is much higher than the noise floor of the pressure probe, which means that the sensor can accurately capture the signals. It is also evident, from measurements of both the test cases, that the pressure sensor is limited by the fact that its sampling frequency is only 1000 Hz. Thus, the information of velocity fluctuations in the turbulent flow that occur at frequencies greater than 1000 Hz is lost.

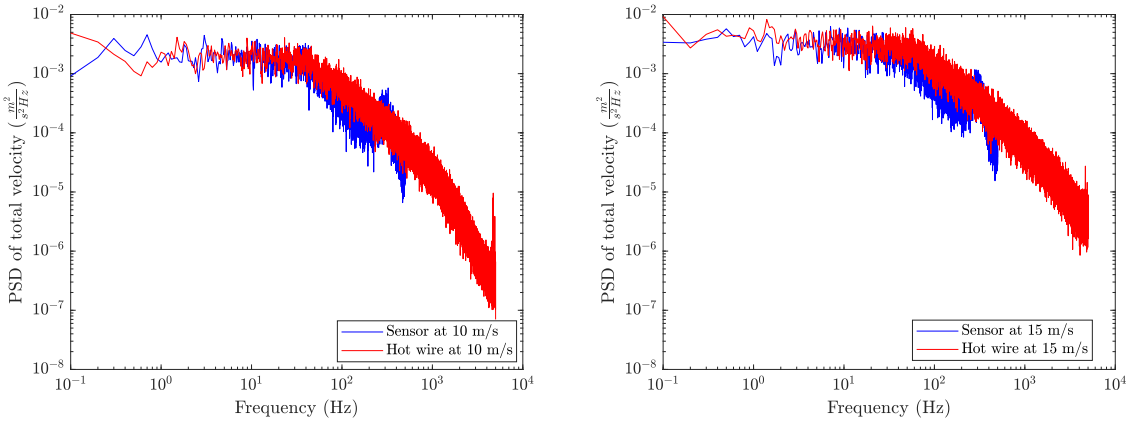

Figure 5.8: PSD of total velocity from probe and hot-wire measurements with turbulence generated using Grid 1

5.4. Balance measurements

To determine the drag on the cylinder, a two-component force balance manufactured in-house is used, and this can be seen in 5.5b. This force balance is made up of three S-shaped load cells of type: KD40s (max range ±50N, max error: ≤ 0:1%). Two of the load cells measure the stream-wise force while the other one measures the lateral force [31]. In this work, drag force is measured using the two load cells that measure the stream-wise force.

The drag force is measured at different flow velocities controlled by the RPM of the centrifugal fan. The measurements are conducted with the tunnel configuration without the grids, as well as for a variety of turbulence levels achieved through the turbulence simulation procedures described in previous sections. The set-up of the force balance and the cylinder model can be found in figure 5.5b. In the case of the smooth cylinder, the measurements are taken between an RPM range of 500-2500 (corresponding to a velocity range of 5 m/s to 25 m/s), with increments of 250. For the rough cylinder, the same procedure is followed, and is supplemented by additional measurements in increments of 100 rpm to get a better resolution of the drag crisis region. This makes it easier to see the shift in the drag crisis region with increasing levels of turbulence.

The data acquisition system consists of a National Instruments NI cDAQ-9178 chassis containing two C-series modules NI-9215 (Voltage Input) and NI-9327 (Strain/ Bridge Gauge). Simply put, this system acquires the electrical signals transmitted by the load cells of the force balance. This data can be read and displayed using

the LabView software. The measurements can be controlled via this software and it directly stores the data onto the computer. The program used with the software outputs data in the form of instantaneous forces measured by the three load cells at a frequency of 50 kHz. The sum of two of these forces corresponding to the two stream-wise load cells is the drag force, from which the drag coefficient can be calculated as shown in equation 2.3.

6

Results and Discussions

This chapter discusses the results of the two experimental campaigns described in Chapter 4 and Chapter 5. In order to do so, it is structured in the following manner. The turbulent flow field encountered by a single rider on the velodrome track is first discussed. Then, the results of the two-rider configuration on track are presented, to understand the effects of riding in the far wake of a leading cyclist. Following this are the results from simulating in a wind tunnel the turbulence levels identified on the velodrome track. The effects of these simulated turbulence levels on the drag of a smooth and rough surfaced cylinder concludes this chapter.

6.1. A single rider in a velodrome

This section delves into the nature of the turbulent flow field generated by an individual rider in the velodrome, riding at a speed of around 45 km/h (12.5 m/s). In order to do so, the time series of flow velocity and flow angles are investigated. This is followed by a spectral analysis of these flow quantities. A comparison of the turbulence spectra at different rider speeds and the flow properties of turbulence, the turbulence intensity and length scales, concludes this section.

6.1.1. Time series

The instantaneous time signal of the total flow velocity, the yaw and pitch angles are visualised in figure 6.1. This time signal corresponds to a single lap completed at a wheel speed of about 45 km/h (12.5 m/s). It can be observed that the variation of yaw and pitch angles are periodic in nature, reliant on the location of the cyclist on the track. At the entry of the bends, it is seen that there is an increase in the yaw angle and the magnitude of the pitch angle. The opposite is true at the exit of the bends, characterised by a reducing yaw angle and magnitude of the pitch angle. These observations are in line with those made by Fitzgerald et. al [28].

6.1.2. Spectral analysis

A spectral analysis of the flow velocities and flow angles for a cyclist riding at a wheel speed of about 45 km/h (12.5 m/s) revealed the presence of some periodic components of the airflow. The following results are obtained from a raw signal gathered

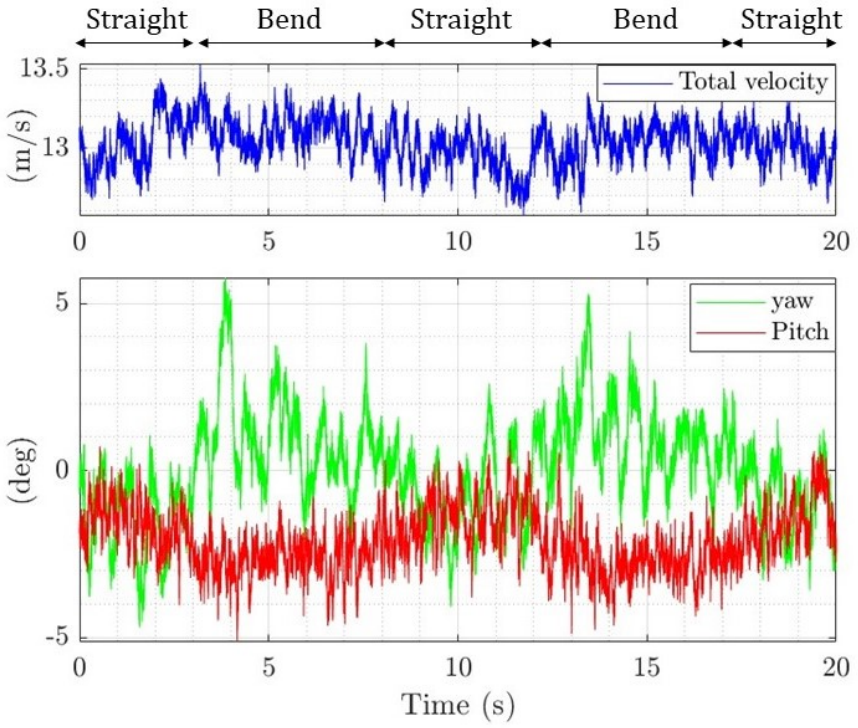

Figure 6.1: Variation of the total velocity, yaw and pitch with time over the course of a single lap

over the course of five full laps around the velodrome track, out of which the data of the first three laps are used for the spectral analysis. Figure 6.2 shows the power spectral density of the total velocity and the u-components of velocity. Two noticeable peaks can be observed in both these figures - one at a frequency of 0.12 Hz, and one at a frequency of 3.42 Hz.

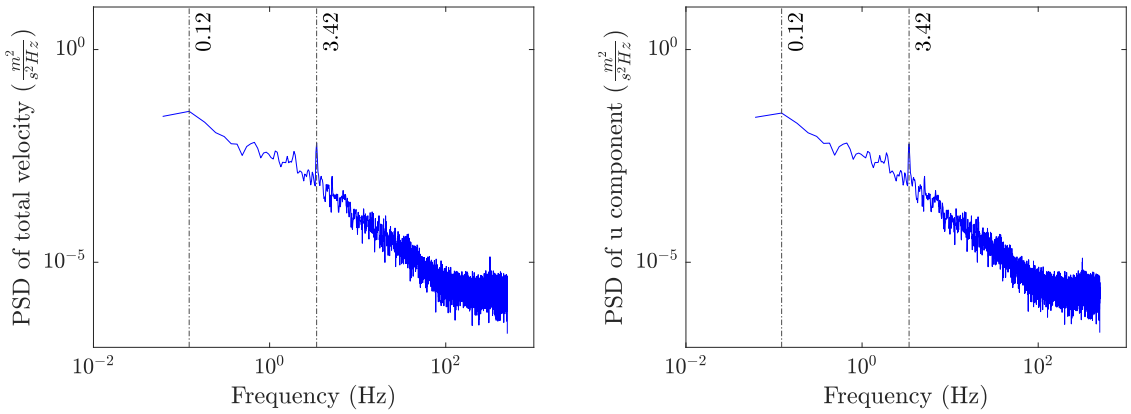

Figure 6.2: The power spectral density of the total velocity (left) and the u-component of velocity (right). In both figures, the first vertical line at 0.12 Hz corresponds to the mean half-lap frequency and the second vertical line at 3.42 Hz corresponds to twice the cadence frequency.

Comparing these results to those of Fitzgerald et. al. [28] reveals that the first peak

corresponds to the mean half-lap frequency and the second peak corresponds to twice the mean cadence frequency. The measured average lap time is around 20 seconds, which gives a mean half-lap frequency of 0.10 Hz as opposed to the frequency of 0.12 Hz that can be seen in these figures. This difference of 20% can be attributed to the low resolution of the sensor at very low frequencies. The measured mean cadence from a cadence sensor is 97.08 rpm as opposed to the cadence of 102.6 rpm that corresponds to a frequency of 1.71 Hz. The difference between the two is less than 6%, implying a clear influence of the cadence cycle on flow field velocity. In the case of the PSD of total velocity and the u-component of velocity, Fitzgerald et. al. [28] theorize that a frequency of twice the cadence frequency is observed due to the forward and vertical motion of each leg.

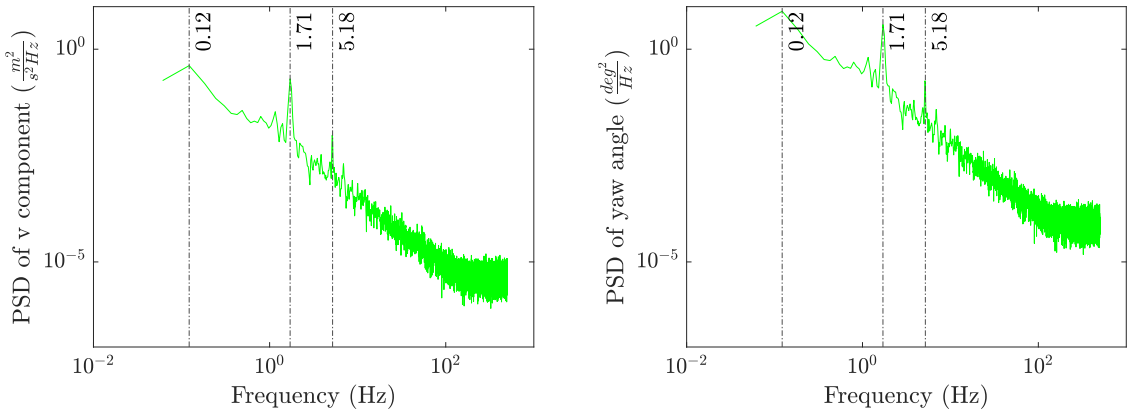

Figure 6.3: The power spectral density of the v-component of velocity (left) and the yaw angle (right). In both figures, the first vertical line at 0.12 Hz corresponds to the mean half-lap frequency; the second vertical line at 1.71 Hz corresponds to the cadence frequency; and the third vertical line at 5.18 Hz corresponds to three times the cadence frequency.

The PSD of the v-component of velocity and the yaw angle are shown in figure 6.3. The two spectra are very similar because of the way the yaw angle is defined (refer to figure 4.4). The first peak observed in these two figures is at 0.12 Hz, similar to figure 6.2, which indicates the mean half-lap frequency. A second peak observed at 1.71 Hz corresponds to the mean cadence of 102.6 rpm. During the course of a pedal cycle, one leg is forwards producing a positive yaw angle and the other, rearwards, producing a negative yaw [28]. This asymmetric upstream effect of the cyclist's legs is reflected as the mean cadence peak in the yaw spectrum. A third peak seen at 5.18 Hz is about three times the mean cadence frequency. The investigations of Fitzgerald et. al. revealed minor peaks at two times and three times of the mean cadence frequency [28]. In the present study, only the latter is found.

Figure 6.4 shows the PSD of the pitch angle and the w-component of the velocity. The only noticeable peak here is that of the mean half-lap frequency. It is clear that there is no dependence of these two flow quantities on the cadence cycle of the cyclist, which is agreement with the literature [28]. A theory proposed by Fitzgerald et. al. to explain the presence of cadence frequency peaks in the yaw spectrum is the rocking and weaving of the bicycle itself due to the pedalling motion of the cyclist. The bicycle

rocks to the left when a cyclist pushes down with their right leg, which results in the tip of the probe to also sweep laterally to the left, inducing a positive yaw angle. This process is mirrored during the second half of the pedal cycle [28]. The pedal cycle thus causes a left-to-right sweeping motion of the sensor, in the x-y plane, which is reflected in the yaw angle measurements. By definition, the pitch angle is defined in the x-z plane (figure 4.4), and the effects of the pedal cycle are therefore not seen in the corresponding pitch spectrum.

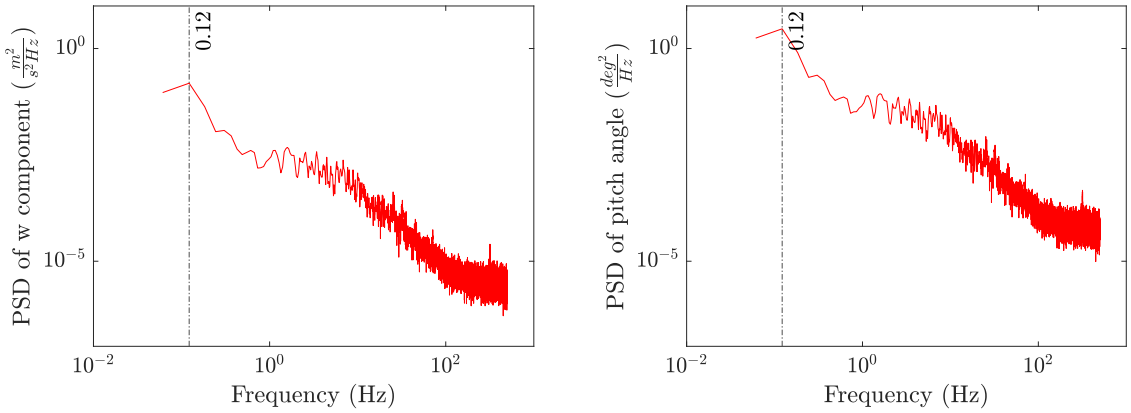

Figure 6.4: The power spectral density of the w-component of velocity (left) and the pitch angle (right). In both figures, the vertical line at 0.12 corresponds to the mean half-lap frequency.

The spectral analysis revealed the existence of periodic components to the flow dependent on the cadence of the cyclist. However, it can also be seen that the amplitudes of these period components are quite insignificant compared to the measured background signal. Moving forward, the presence of these cadence peaks are noted but not considered in the attempts to recreate this turbulent flow field in a wind tunnel.

6.1.3. Turbulence measured at varying rider speeds

Figure 6.5 presents the turbulence spectrum of the velocity magnitude for three different wheel speeds of the cyclist. As expected, the energy content of the flow field increases with increasing velocity. The periodic components observed at a rider speed of 12.5 m/s (45 km/h) were also observed in the spectra obtained at the other two rider velocities. The peaks corresponding to two times the cadence frequency are highlighted in figure 6.5. It can be seen that with an increase in rider velocity, the frequency also increases. This is a result of the cyclist using a fixed gear throughout the tests, which means an increase in cadence is observed as the speed increases. The peaks corresponding to the mean half-lap time are observed at 45 km/h and 55 km/h. However, its validity cannot be confirmed owing to the poor resolution of the sensor at very low frequencies. As discussed in section 6.1.2, these cadence-related frequencies are also observed in the PSD of the velocity components and flow angles. For the sake of brevity, the PSD of velocity components are presented in Apendix A, with the PSD of yaw and pitch being similar to the v and w component of velocity.

Table 6.1 provides the details of the turbulence intensity, RMS velocity fluctuations and integral length scales measured at these three rider velocities. The strength of

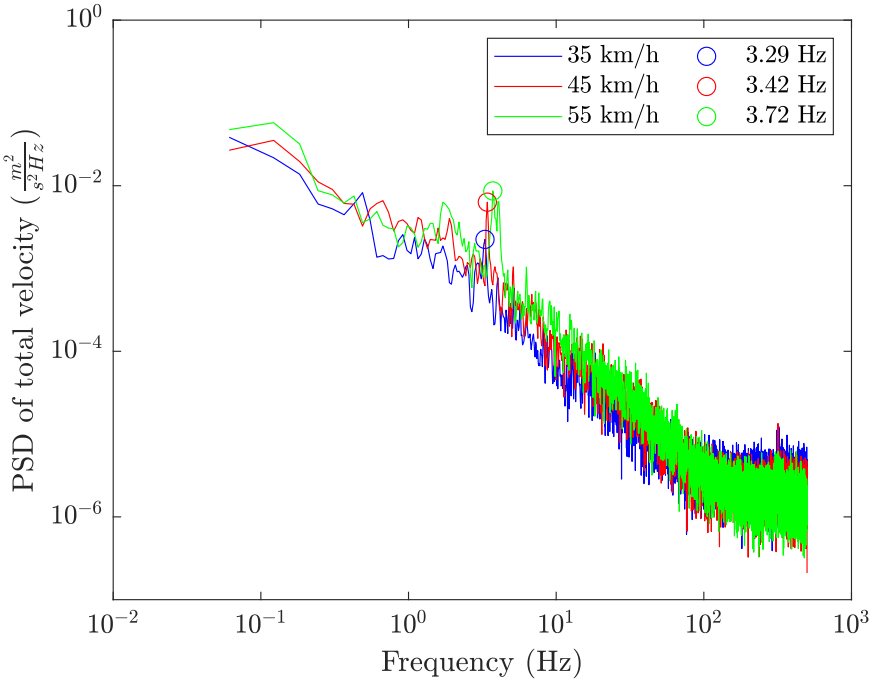

Figure 6.5: Comparison of the power spectral density of total velocity for different rider speeds

the turbulence is expected to increase monotonically with the cyclist's speed. This is reflected in the RMS of velocity fluctuations U_{RMS}. Since the turbulence intensity (T.I) is a ratio of these RMS velocity fluctuations to the mean flow speed, the increase in turbulence that is expected is not seen readily as in the case of U_{RMS}.

Turbulence flow property	35 km/h	45 km/h	55 km/h
T.I (%)	1.18	1.05	1.19
U_{RMS}	0.11	0.13	0.18
$\Lambda(m)$	2.36	1.36	2.81

Table 6.1: Turbulence intensity (T.I), RMS velocity fluctuations (U_{RMS}) and Integral length scale (Λ) at different rider speeds

6.2. Turbulence encountered by a trailing cyclist

To determine the effect of a cyclist riding in the far wake of a lead cyclist, the flow turbulence was measured at three different rider separation distances - half a lap, quarter of a lap, and one eighth of a lap, at a constant rider speed of 12.5 m/s (45 km/h). The resulting turbulence spectra of the velocity magnitude, compared with that of the turbulence generated by a single rider on track at the same wheel speed are presented in figure 6.6. It can be seen that the lowest level of turbulence is generated by the presence of the single rider on track (given by the black curve), while the highest level of measured turbulence is found when the distance of separation between the riders

is one eighth of a lap. There appears to be not much of a difference between the turbulence spectra measured at the other two separation distances, although the turbulence measured at a quarter of a lap seems marginally lower in spectral content than that measured at a separation of half a lap, probably due to measurement uncertainties. It is also noticeable that the cadence related peak observed with an isolated rider is not noticeable when riding in the wake of a lead rider. As mentioned previously, these cadence peaks have very low amplitude and are hence ”hidden” by the turbulent fluctuations caused by the lead rider.

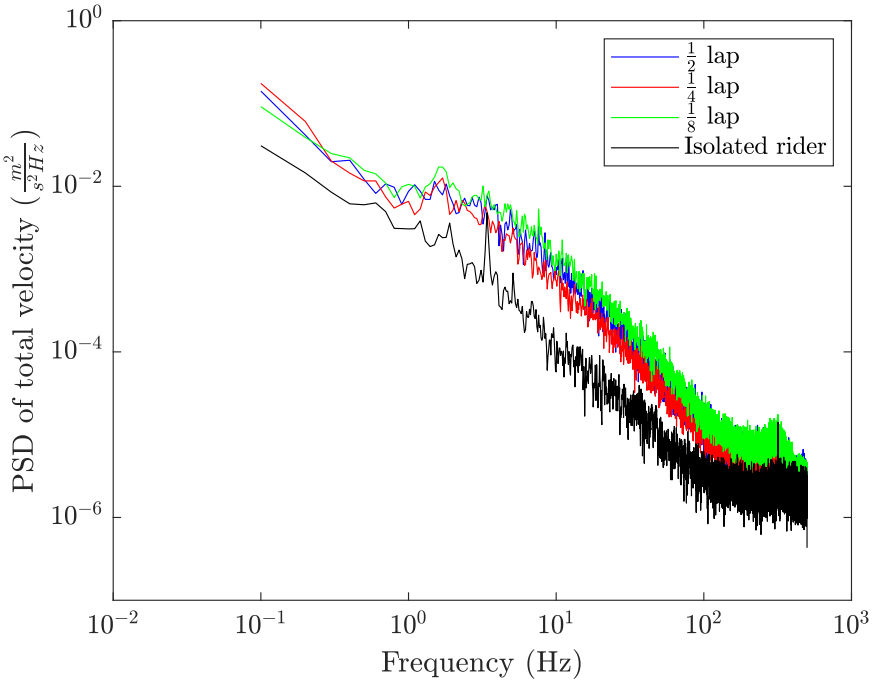

Figure 6.6: Comparison of the power spectral density of total velocity at varying separation distances between the lead and the trailing cyclist

The turbulence intensities, RMS velocity fluctuations and integral length scales measured at these three separation distances can be found in table 6.2. As expected, the isolated rider encounters the least intensity of turbulence. The wake of a cyclist disperses with increasing downstream distance. This means that the strength of the turbulence encountered by a trailing cyclist at a larger distance away from the lead cyclist is weaker, and this is seen clearly in the values of turbulence intensity and RMS of velocity fluctuations. It can be seen that when the lead rider is half a lap away from the trailing rider, the highest value of integral length scale is observed. No clear trend of the change in length scale with varying distance is found.

6.3. Wind tunnel measurements

This section delves into the results of the wind tunnel investigations conducted post the analysis of the turbulent flow field measured in the velodrome. The first part of this section deals with the simulated turbulence in the wind tunnel, and to what extent this simulated turbulence matches the turbulence spectra and turbulence intensities

Turbulence flow property	Isolated rider	$\frac{1}{2}$ lap	$\frac{1}{4}$ lap	$\frac{1}{8}$ lap
T.I (%)	1.05	2.07	2.16	2.58
U_{RMS}	0.13	0.27	0.28	0.33
$\Lambda(m)$	1.36	8.92	0.78	1.16

Table 6.2: Turbulence intensity (T.I), RMS velocity fluctuations (U_{RMS}) and Integral length scale (Λ) at different separation distances

measured in the velodrome. Following this, the effects of this simulated turbulence on the drag crisis of a smooth and rough surfaced cylinders are elaborated upon.

6.3.1. Turbulence simulation in a wind tunnel

It was previously mentioned that the exact replication of a turbulence spectrum and turbulence intensity is somewhat difficult. For this reason, the lowest and highest spectral content of turbulence measured in the velodrome, that is, the case of turbulence encountered by a single cyclist on track and by a trailing cyclist following the lead cyclist at a distance of an eighth of a lap, are used as the lower and upper limits for the target spectrum that is to be achieved. Using the experimental set-up for the simulation of turbulence discussed in Chapter 4, several combinations of grids placed at the inlet of the test section, with and without the presence of cylinders of varying square cross sections in the settling chamber, were thoroughly tested and compared to the velodrome data. For the sake of brevity, the turbulence spectra that were the closest match to the lower and upper limits will be discussed here. The rest of the results obtained are presented in Appendix B.

Name	Description
Config 1	No grid (in blue)
Config 2	Grid 2 at the inlet of the test section (in green)
Config 3	Two square beams fitted side-by-side in the settling chamber (in yellow)
Config 4	A combination of Config 2 and Config 3 (in red)

Table 6.3: A description of the 4 main experimental configurations used in the simulation of turbulence

Figure 6.7 shows the turbulent spectra obtained from the four configurations (table 6.3) of the experimental set-up that are most relevant to this discussion. The blue curve represents the base turbulence levels measured in the wind tunnel in the absence of any grids or objects that generate turbulence. This measured turbulence energy is much lower than the velodrome turbulence levels, with the energy at lower

frequencies being almost two decades lower than in the case of the upper limit of the velodrome turbulence. This observation holds at both the wind tunnel flow speeds. The turbulence generated by Grid 2 (in green) offers some similarity to the lower limit of the expected turbulence levels at frequencies greater than 10 Hz, but not at frequencies lower than 10 Hz. A noticeable difference between the spectra at 10 m/s and 15 m/s in the case of Grid 2 is the jump in the measured energy at 15 m/s that is quite significant when compared to the other configurations tested. At 15 m/s, the energy levels at frequencies greater than 10 Hz are closer to the upper limit of the velodrome turbulence.

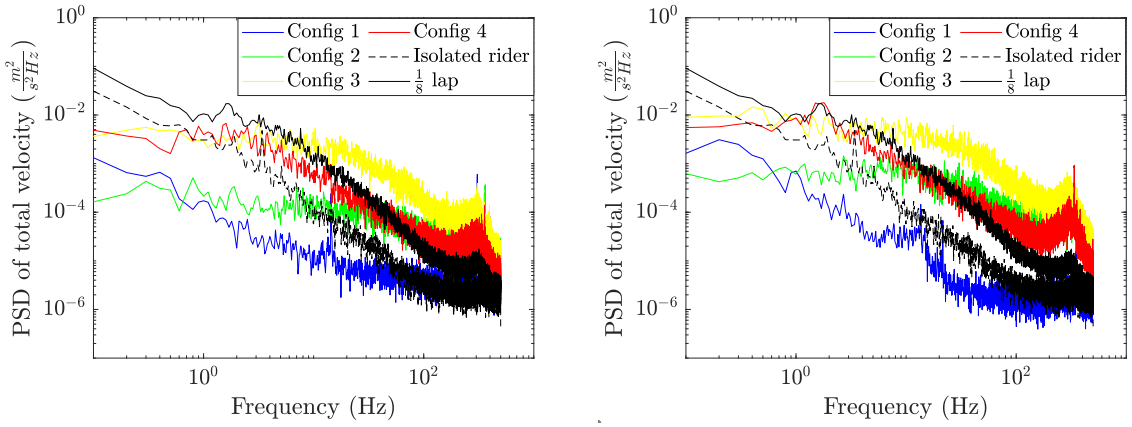

Figure 6.7: A comparison of turbulence spectra obtained from 4 different configurations (See table 6.3 for the descriptions) with the lower and upper levels of turbulence measured in a velodrome at a rider speed of 12.5 m/s. On the left is the spectra obtained at a wind tunnel velocity of 10 m/s, and on the right are spectra obtained at a wind tunnel velocity of 15 m/s.

The energy of the turbulence simulated is higher when using just the beams in the settling chamber, as seen with the yellow curve. The beams provide a large cross-section, promoting large scales of turbulence, as opposed to turbulence generated due to a grid. This configuration offers the expected level of energy at frequencies less that 10 Hz. However, the turbulence energy is higher than the upper limit of the measured velodrome turbulence at frequencies greater than 10 Hz. Using a combination of the grid and the beams creates a turbulence spectrum that falls between the limits of that of the velodrome turbulence from a range of 1 Hz to almost 100 Hz (depicted by the red curve). This particular combination is therefore considered the best method to simulate properly the conditions measured in the velodrome and the turbulence generated via this method is investigated further.

Table 6.4 and table 6.5 provide the information on the intensities, RMS velocity fluctuations and integral length scales at 10 m/s and 15 m/s respectively. As expected, config 1, with no turbulence generating mechanisms, provides the least turbulence intensities and length scales. the highest turbulence intensities are measured when using config 3, the beams in the settling chamber. Using config 4 provides a turbulence intensity in between that of config 2 and 3. This set-up also generates the highest integral length scale in the wind tunnel. This is due to the fact that the cross-section of the wind tunnel test section is not large enough to replicate the large scale of turbulence that is encountered on track.

Config	T.I (%)	U_{RMS}	$\Lambda(m)$
1	0.41	0.04	0.0053
2	1.56	0.14	0.0062
3	3.54	0.36	0.0402
4	2.02	0.21	0.1501

Table 6.4: Turbulence intensity (T.I), RMS velocity fluctuations (U_{RMS}) and Integral length scale (Λ) obtained from different methods of turbulence simulation at a wind tunnel speed of 10 m/s

Config	T.I (%)	U_{RMS}	$\Lambda(m)$
1	0.43	0.06	0.0084
2	1.71	0.24	0.0153
3	3.28	0.51	0.0466
4	1.72	0.27	0.2250

Table 6.5: Turbulence intensity (T.I), RMS velocity fluctuations (U_{RMS}) and Integral length scale (Λ) obtained from different methods of turbulence simulation at a wind tunnel speed of 15 m/s

In order to have a better match to the measured turbulence levels, the turbulence simulated using the grid and the beams in combination at a wind tunnel velocity of 12.5 m/s, which is the same as the average wheel speed of the cyclist, is presented in figure 6.8. The turbulence intensity and length scales measured using this configuration are compared to the target levels measured in the velodrome in table 6.6. While the turbulence intensity falls between the lower and upper limits of the velodrome turbulence intensities, it can be seen that the integral length scale generated in the wind tunnel is much smaller than that measured on track, which is to be expected due to the size of the wind tunnel and the test section itself.

Turbulence flow property	Isolated rider	$\frac{1}{8}$ lap	Config 4
T.I (%)	1.04	1.94	1.78
U_{RMS}	0.13	0.24	0.22
$\Lambda(m)$	1.36	1.16	0.15

Table 6.6: Turbulence intensity (T.I) and Integral length scale (Λ) of the lower and upper limits of measured velodrome turbulence and for Config 4 at 12.5 m/s

Figure 6.9 shows the PSD of the u component and v component of the velocities at a wind tunnel speed of 12.5 m/s in comparison with the velodrome turbulence. It can be seen that the spectrum of the u component of the velocity offers a good match to the velodrome turbulence levels, similar to the spectrum of the total velocity. On the other hand, the energy of v component of the velocity is not a good match for even the lower limit of the measured turbulence at frequencies less than 10 Hz. At higher frequencies, it seems to match the turbulence spectrum of the isolated rider in

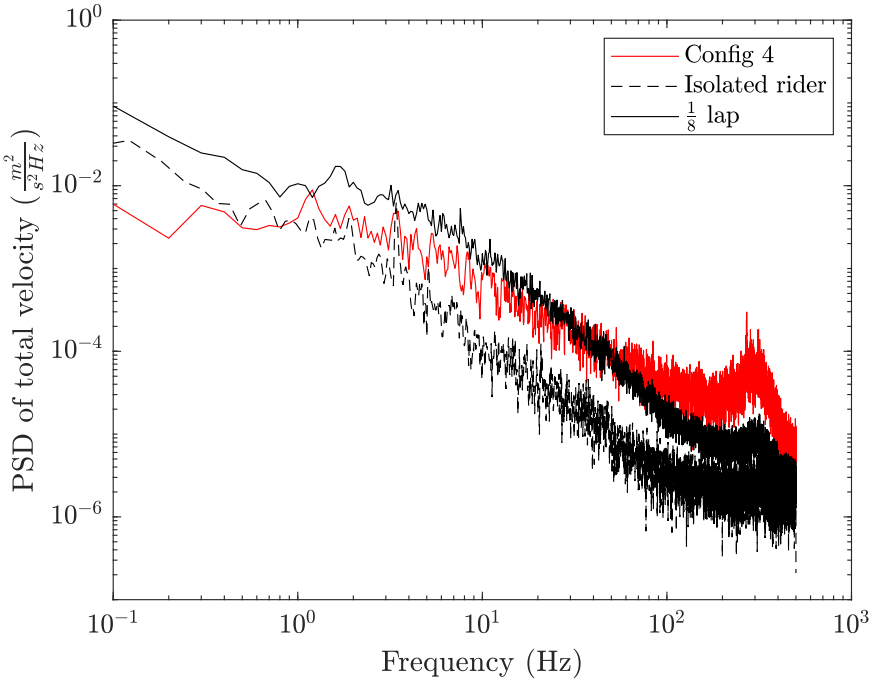

Figure 6.8: Power spectral density of the total velocity compared to the lower and upper limits of the measured velodrome turbulence at a wind speed similar to the wheel speed of the cyclist in the velodrome (12.5 m/s)

the velodrome. This can be attributed to the orientation of the large obstacle in the settling chamber, which generates larger scales in the streamwise direction but no so much in the lateral direction. Table 6.7 provides the values of intensities, integral length scale, and RMS values of velocity fluctuations in the streamwise and lateral directions.

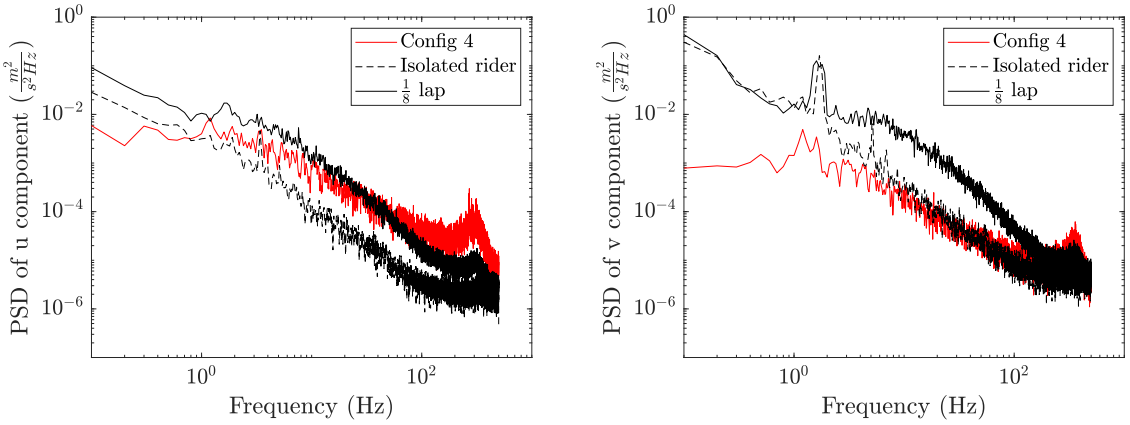

Figure 6.9: Power spectral density of the u component and the v component of the velocity compared to the lower and upper limits of the measured velodrome turbulence at a wind speed similar to the wheel speed of the cyclist in the velodrome (12.5 m/s)

Turbulence flow property	Isolated rider	$\frac{1}{8}$ lap	Config 4
$T.I_x$ (%)	1.03	2.64	1.77
u_{RMS}	0.13	0.34	0.23
$\Lambda_x(m)$	1.32	1.23	0.13
$T.I_y$ (%)	2.62	1.04	0.96
v_{RMS}	0.34	0.51	0.12
$\Lambda_y(m)$	1.78	0.61	0.12

Table 6.7: Turbulence intensity (T.I) and Integral length scale (Λ) of the lower and upper limits of measured velodrome turbulence and for Config 4 at 12.5 m/s, for the u and v components of velocity

6.3.2. Drag measurements on circular cylinders

The results of the drag force measured on a smooth surfaced circular cylinder in the presence of the previously discussed simulated turbulence levels are presented in figure 6.10, in the form of a drag coefficient vs the flow velocity, Reynolds number plot. It can be seen that in the absence of a turbulence generating mechanism, the C_D falls between 1 and 1.1 for the entire range of flow velocities tested (given by the blue curve). This indicates that the critical Re is not reached, and the cylinder is still in the subcritical flow regime. In the case of turbulence generated using Grid 2, represented by the green curve, the drag coefficient measured is higher than in the absence of a grid below a flow velocity of about 12.5 m/s, after which it marginally drops below the blue curve.

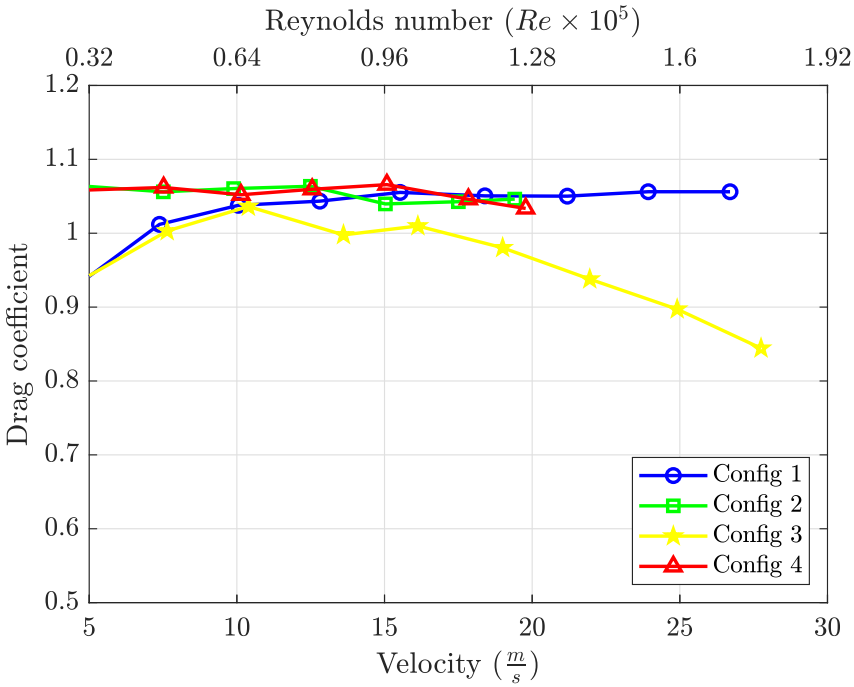

Figure 6.10: Drag coefficient vs Velocity, Reynolds number for a smooth surfaced cylinder. Refer to table 6.3 for a description of the legend.

Generating turbulence using the beams in the settling chamber produces the highest intensity of turbulence amongst all the tested configurations. The drag of a smooth cylinder under this flow is given by the yellow curve and it can be seen that the drag curve follows the trend of the blue curve up to 10 m/s, after which there is a marginal drop in C_D between 10 m/s and 12.5 m/s. The C_D value remains more or less constant between 12.5 m/s and 15 m/s, after which a steady decrease in C_D is observed. The cylinder is in the critical flow regime. In the case of the smooth surfaced cylinder, it seems that a turbulence intensity of about 3.2% - 3.4% is sufficient to result in a reducing C_D. Finally, in the case of turbulence simulated using the grids and the beams together (config 4) results in a drag curve (red) similar to that of config 2.

Figure 6.11 shows the C_D curves for a rough surfaced cylinder in the presence of varying turbulence levels. The blue curve, representing the case of the absence of turbulence generation techniques, shows C_D values ranging from 0.95 to about 1.05 for velocities less than 12 m/s. Between 12 m/s and 13 m/s, the C_D drops steeply to a value of 0.68, after which the C_D increases gradually to a value of 0.9 at 27.5 m/s. The surface roughness induces an early transition, which causes a flow separation below $Re = 10^5$, and hence drag crisis as opposed to the smooth surfaced cylinder which remains in the subcritical regime.

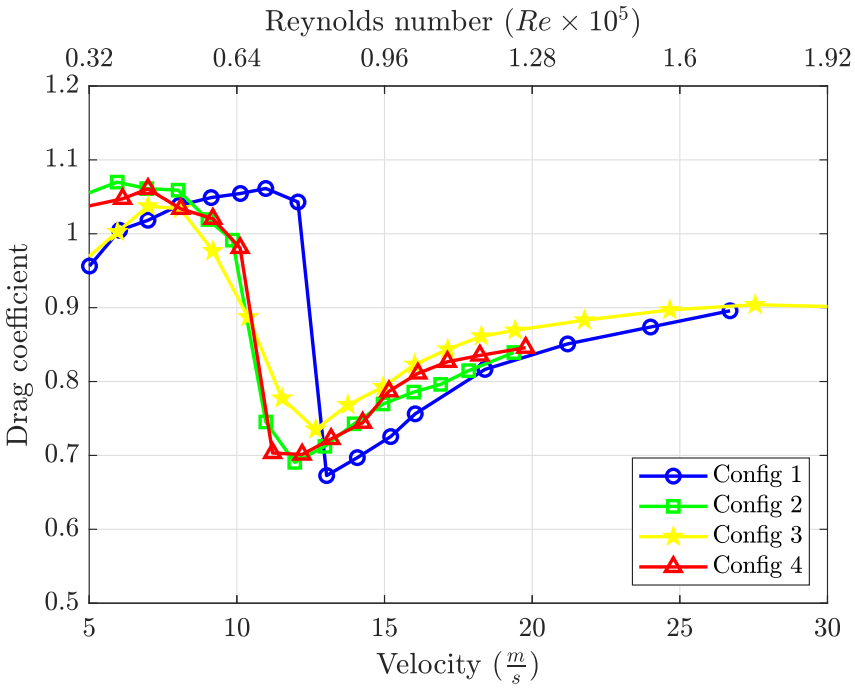

Figure 6.11: Drag coefficient vs Velocity, Reynolds number for a rough surfaced cylinder. Refer to table 6.3 for a description of the legend.

When turbulence is simulated using grid 2, the C_D values follow the green curve. The value of C_D is initially higher than what is measured under no simulated turbulence, but starts decreasing gradually at a flow velocity of 8 m/s until 10 m/s. From 10 m/s to 12 m/s, the C_D reduces comparatively faster until it reaches a minimum of 0.7. Beyond this, it increases again to reach a value of 0.85 at a velocity of 19 m/s.

The yellow curve, representing turbulence simulated using beams in the settling

chamber, is similar to the blue curve below 8 m/s, after which the C_D drops very gradually over a range of velocities, to reach a minimum of 0.72 at 13 m/s. After this, the C_D gradually increases again to a value of 0.9 at 27.5 m/s. In the case of the turbulence generated using both the grid and the beams, the C_D curve is represented by the red curve. This drag curve follows a similar trend to the green curve. The few minor differences that can be noted are that the C_D is minutely lower at velocities lower than 7 m/s, and the minimum C_D occurs over a range of velocities between 11 m/s and 12 m/s. Between the velocities of 15 m/s and 18 m/s, the C_D is marginally higher.

This drag analysis provides several insights on the effects of free stream turbulence and surface roughness. In the case of the smooth cylinder, the high turbulence intensity produced by the beams in the settling chamber (table 6.4, 6.5) was sufficient to promote flow transitions and decreasing C_D. When the full measured spectrum is simulated using the grid and the beams, the drag curve obtained was very similar to the one obtained when turbulence was generated using only grid 2. It can be inferred that small scale turbulence produced by the grid has more of an effect on the drag of the smooth cylinder than the large scale structures produced using a combination of the grid and the beams.

Drag crisis can also be achieved using surface roughness to trigger flow transitions, as seen in the case of the rough cylinder in the absence of turbulence generating mechanisms [1]. A combination of free stream turbulence and surface roughness promotes drag reduction at lower speeds. The range of critical Re is larger when the two ”disturbances” are simultaneously in play, the largest range of which is noticeable when generating turbulence using Config 3 (7.5 m/s - 12.5 m/s). However, the value of minimum C_D is higher when turbulence is also considered. Beyond drag crisis, the drag experienced by a rough cylinder in the presence of turbulence is also higher. Similar to the smooth cylinder, it is observed that the drag curves of the rough cylinder in turbulent flow generated by config 2 and 4 are very similar.

7

Conclusions and Recommendations

7.1. Conclusions

At the outset of this thesis, a series of research questions, (section 2.5) were posed to gain a better understanding of the effect of turbulence levels measured in an indoor velodrome on the aerodynamic drag of a cyclist. The wind turbulence measurements in speed skating and the subsequent wind tunnel simulations to determine the effects on the drag coefficient of a speed skater by D'Auteuil et. al. established the need to factor real flow conditions to obtain relevant drag results in the wind tunnel [21]. Since cyclists and speed skaters operate in the same Reynolds number regimes, it is safe to infer that the drag of a cyclist will also react to free stream turbulence. Experimental investigations conducted in the velodrome, and subsequently in the wind tunnel yielded conclusive results which are presented in this chapter.

What are the turbulence intensities and spectra encountered by a cyclist in an indoor velodrome ?

The measurements in the velodrome were broadly divided into two categories - the turbulence encountered by an individual cyclist on track, and the turbulence encountered when riding in the far-wake of a leading cyclist. These turbulent velocity fluctuations generated in the velodrome were measured using a three-hole pressure probe from AeroLab Tech, Canada. In the case of the individual cyclist, the time series of the total velocity, yaw and pitch signals over a single lap showed the dependence of the airflow on the cyclist's location on track, similar to the observations of Fitzgerald et. al. [28]. A spectral analysis of these time signals revealed the presence of periodic components which were a result of the cadence of the cyclist. Again, these observations re-affirm the results obtained by Fitzgerald et. al. [28]. A comparison of the turbulence spectra, intensities, RMS velocity fluctuations and length scales at different rider speeds (35 km/h, 45 km/h, 55 km/h) showed that the strength and energy of the turbulence increases monotonically with rider speed. The relation between the length scales and rider speeds could not be ascertained.

While the work of Fitzgerald et. al. also examined the turbulence intensities encountered at different rider positions in a team pursuit [28], information on the effect of far-wakes was missing in literature. Examining these far-wake effects could be ben-

eficial in track cycling events like the individual pursuit. In this thesis, the turbulence encountered by a trailing cyclist separated from the lead cyclist by half a lap, quarter of a lap, and one eighth of a lap were measured at a speed of 45 km/h. The intensity of the turbulence was higher as the distances got smaller - measuring 2.07%, 2.16%, and 2.58% at half a lap, quarter of a lap and an eighth of a lap respectively. The turbulence spectra obtained had the highest energy content at a separation of one-eight of a lap. The energy content measured at quarter of a lap was marginally lower than at half a lap, owing to measurement uncertainties. The integral length scale of turbulence presented the highest value at half a lap - 8.92 m, and the lowest at quarter of a lap - 0.78 m, which is also lower than the length scale measured with an isolated rider - 1.36 m. While the results of this study suggest a certain outcome with the integral length scales, further research is needed to confirm these findings.

How can these measured turbulence levels be replicated in a wind tunnel ?

To simulate the turbulence spectra and intensities measured in the velodrome, passive methods of turbulence generation in wind tunnels were used. Since the replication of the exact levels of turbulence intensities and spectra is difficult, the lowest measured turbulence in the velodrome (isolated rider) and the highest measured turbulence (at a distance of an eighth of a lap) were chosen as the lower and upper limits for the target spectrum and intensity generated in the wind tunnel. Several combinations of grids placed at the inlet of the test section and large obstacles placed in the settling chamber were tested in a trial-and-error based approach to arrive at the best method to simulate the required turbulence levels.

A combination of a perforated plate of dimensions mesh length $M = 5mm$, hole diameter $d = 2mm$ and porosity $\beta = 0.12$ placed at the inlet of the test section and a cylinder of rectangular cross-section of 95 mm $\times$ 190 mm placed in the settling chamber (Config 4) produced a turbulence spectrum that falls within the required velodrome limits. The intensity of turbulence simulated was 1.78%, which also lies between the upper and lower limits of 1.94% and 1.04% respectively. The integral length scale of turbulence generated, however, was lower by a factor of nearly 10. This was to be expected due to the relatively small wind tunnel test section used in this thesis. Further analysis of the spectrum in the longitudinal and lateral directions revealed that while the PSD of the u-component of velocity lies within the velodrome limits, the PSD of the v-component matches the lower limit only at frequencies greater than 10 Hz. At lower frequencies, the energy of this spectrum was smaller by almost two decades. It is possible that this is due to the orientation of the large obstacle in the settling chamber, which is responsible for generating large scale, low frequency turbulence.

What are the effects of this measured turbulence on the drag crisis of a circular cylinder ?

The changes in drag coefficient of a smooth and rough surfaced cylinder over a range of flow velocities (5 m/s - 25 m/s) were examined in four different turbulent flows. First, in the case of flow in the wind tunnel without turbulence generating mechanisms (Config 1) with turbulence intensity of about 0.4%, the smooth cylinder exhibits a near con-

stant C_D of 1.05. With turbulence from Config 2 (perforated plate at the inlet of the test section) and Config 4 (large obstacle in the settling chamber and grid at inlet), the smooth cylinder is still in the subcritical regime, but the C_D at flow speeds less than 13 m/s is higher than in Config 1. The two configurations produce a similar turbulence intensity of about 1.7% at a flow speed of 15 m/s. Config 3 produces a turbulence intensity of around 3.3% at 15 m/s. The flow transition is triggered in the smooth cylinder and the C_D drops after 10 m/s. It is clear that higher turbulence intensity is sufficient to trigger transition. It is also inferred that large scale turbulence has minimal effect on the drag of a smooth cylinder. It is to be noted that these length scales are not an accurate representation of those measured in the velodrome.

Surface roughness causes drag crisis in the case of minimal turbulence as in Config 1. It is seen that the critical Re range is quite small, between flow velocities of 12 m/s and 13 m/s approximately. When both free stream turbulence and surface roughness are present as ”disturbances” to the flow, a few differences are observed in the drag curve when compared to that of Config 1. Flow transitions are triggered much earlier, at around 8 m/s, and the range of critical Re are larger. Especially in the case of flow turbulence caused by Config 3, the critical regime seems to span across a velocity range of around 6 m/s to 12 m/s. The minimum C_D attained is higher compared to Config 1, and so is the C_D in the post critical flow regimes. As in the case of a smooth cylinder, the full turbulent spectrum obtained from Config 4 and the low scale turbulence produced by Config 2 result in very similar drag curves of the rough cylinder.

The testing of cycling skin-suits rarely account for the flow turbulence encountered in real cycling conditions, as revealed in the literature review. As a general rule in the design of skin-suits, first proposed by Brownlie et. al. [13], body parts of a cyclist that are oriented with the flow direction with attached flow, such as the torso, are covered in smoother fabrics to minimise the shear forces. The body parts in cross-flow, like the upper arms and thighs, are covered in rough fabrics to trigger flow transitions so as to reduce the pressure drag. If flow transitions are triggered in smooth fabrics in the presence of free stream turbulence, as in the case of Config 3, then perhaps they could be used on body parts in cross-flow. Since the drag measurements in this thesis were conducted with the cylinder oriented vertical to the wind tunnel flow, it is difficult to ascertain if FST has an effect on smooth fabrics used over body parts aligned with the flow. While only one rough fabric was tested in this thesis, it is clear that FST triggers early transition, and the minimum C_D obtained is higher than what is typically obtained in a wind tunnel. A possible result of this observation is that the flow transition occurs prematurely at competitive events as opposed to the expected Re range, thereby not offering the expected drag reductions.

7.2. Recommendations

While the experimental investigations of this thesis provided a look into the effects of free stream turbulence in cycling aerodynamics - specifically skin-suits, several improvements could be implemented in future research to obtain a much accurate understanding of the inherent flow experienced by a cyclist in race conditions, and subsequently adjusting the wind tunnel turbulence levels to obtain relevant results.

- It was difficult to ascertain the vibrations of the sensor on the velodrome track due to the low sampling frequency of the available accelerometer (which is a part of the 40 Hz AeroPro sensor). Therefore, an accelerometer with a higher sampling frequency could be used to determine these vibrations.
- The velocity fluctuations of the turbulent flow was measured by a three-hole pressure probe, which only provides velocity in two dimensions. The probe also sampled at a frequency of only 1000 Hz. It would be beneficial to use a multi-hole probe capable of measuring velocity fluctuations in three dimensions, as well as one with a higher sampling rate to capture turbulent fluctuations at higher frequencies.
- When it comes to the simulation of turbulence, a better ”large obstacle” could be constructed instead of just two square beams fixed side by side.
- To ascertain the effects of increasing FST on increasing surface roughness, fabrics of different surface roughness could be tested. Also, providing a quantitative estimates of the surface roughness would be helpful.
- The present study is focused on the far wake of a single leading cyclist. Possible extensions to this study include testing with a team pursuit format as opposed to the format of individual pursuit used presently. Specifically, the wakes of an opposing team of cyclists, so to speak, and their effects on the trailing team of cyclists. It can be anticipated that the turbulence generated in that case would be higher than what is measured in this thesis.

Bibliography

[1] E. Achenbach. “Influence of surface roughness on the cross-flow around a circular cylinder”. In: *Journal of fluid mechanics* 46.2 (1971), pp. 321–335.

[2] E. Achenbach and E. Heinecke. “On vortex shedding from smooth and rough cylinders in the rande of Reynolds numbers 6×10^3 to 5×10^6”. In: *Journal of fluid mechanics* 109 (1981), pp. 239–251.

[3] AeroLab. *AeroLab Tech*. 2023. URL: `https://aerolink.tech/` (visited on 02/21/2023).

[4] Ed.) Ames reseach center (K. Aldenbrook. *National Aeronautics and Space Administration*. 2022. URL: `https://www.nasa.gov/centers/ames/orgs/aeronautics/windtunnels/balance-basics.html` (visited on 04/14/2023).

[5] J.D. Anderson. *Fundamentals of Aerodynamics*. McGraw hill, 2011.

[6] N. Barry et al. “The effect of spatial position on the aerodynamic interactions between cyclists”. In: *Procedia Engineering* 72 (2014), pp. 774–779.

[7] R.I. Basu. “Aerodynamic forces on structures of circular cross section. Part 2. the influence of turbulence and three-dimensional effects”. In: *Journal of wind engineering and industrial aerodynamics* 24 (1986), pp. 35–59.

[8] P.W. Bearman and T. Morel. “Effect of free stream turbulence on the flow around bluff bodies”. In: *Progress in Aerospace sciences* 20.2-3 (1983), pp. 97–123.

[9] M. Bellioli et al. “Drafting effect in cycling : investigation by wind tunnel tests”. In: *Procedia Engineering* 147 (2016), pp. 38–43.

[10] B. Blocken et al. “CFD simulations of the aerodynamic drag of two drafting cyclists”. In: *Computers & Fluids* 71 (2013), pp. 435–445.

[11] C. Brown et al. “Understanding the aerodynamic benefits of drafting in the wake of cyclists”. In: *Proceedings* 49.1 (2020), p. 32.

[12] L. Brownlie. “Aerodynamic characteristics of sports apparel”. In: *PhD Dissertation, School of Kinesiology, Simon Fraser University, Burnaby BC, Canada* (1992).

[13] L. Brownlie et al. “Streamlining the time trial apparel of cyclists : The Nike swift spin project”. In: *Sports Technology* 2 (2009), pp. 53–60.

[14] D.W. Bryer and R.C. Pankhurst. “Pressure-Probe Methods for Determining Wind Speed and Flow Direction”. In: *London: Her Majesty’s Stationary Office* (1971).

[15] G. Buresti. *Elements of fluid dynamics*. Vol. 3. World Scientific Publishing Company, 2012.

[16] H. Chowdhury. “Aerodynamic design of sports garments”. In: *Applied Aerodynamics* (2012), pp. 21–40.

[17] H. Chowdhury, F. Alam, and A. Subic. “Aerodynamic performance evaluation of sports textile”. In: *Procedia Engineering* 2 (2010), pp. 2517–2522.

[18] G. Comte-Bellot. “Hot-wire anemometry”. In: *Annual review of fluid mechanics* 8.1 (1976), pp. 209–231.

[19] T. N. Crouch et al. “Riding against the wind: a review of competition cycling aerodynamics”. In: *Sports Engineering* 20 (2017), pp. 81–110.

[20] T.N. Crouch et al. “Flow topology in the wake of a cyclist and its effect on aerodynamic drag”. In: *Journal of Fluid Mechanics* 748 (2014), pp. 5–25.

[21] A. D’Auteuil, G.L. Larose, and S.J. Zan. “Wind turbulence in speed skating : Measurement, simulation and its effect on aerodynamic drag”. In: *Journal of Wind Engineering and Industrial Aerodynamics* 104 (2012), pp. 585–593.

[22] A. D’Auteuil, G.L Larose, and S.J. Zan. “Relevance of similitude parameters for drag reduction in sport aerodynamics”. In: *Procedia Engineering* 2.2 (2010), pp. 2393–2398.

[23] J.F. Derakhshandeh and Md M. Alam. “A review of bluff body wakes”. In: *Ocean engineering* 182 (2019), pp. 475–488.

[24] A.G. Edwards and W.C. Byrnes. “Aerodynamic characteristics as determinants of the drafting effect in cycling”. In: *Med. Sci. Sports Exerc.* 39 (2007), pp. 170–176.

[25] A. Fage and J.H. Warsap. “The effect of turbulence and surface roughness on the drag of a circular cylinder”. In: *Aero. Res. Com. London, R. M.* 1283 (1930).

[26] Z. Fan. “Measurement of aerodynamic forces and moments in wind tunnels”. In: *Encyclopedia of Aerospace Engineering* (2010).

[27] S. Fitzgerald. “Understanding the aerodynamic environment in track cycling”. In: *PhD thesis, The University of Adelaide* (2022).

[28] S. Fitzgerald et al. “Measurement of the air velocity and turbulence in a simulated track cycling team pursuit race”. In: *Journal of Wind Engineering and Industrial Aerodynamics* 190 (2019), pp. 322–330.

[29] M.D. Griffith et al. “Computational fluid dynamics study of the effect of leg position on cyclist aerodynamic drag”. In: *Journal of Fluids Engineering* 136.10 (2014), p. 101105.

[30] J. Hoffman et al. “Effect of test section configuration on aerodynamic drag measurements”. In: *SAE Transactions* 110 (2001), pp. 680–694.

[31] M. Huang, A. Sciacchitano, and C. Ferreira. “On the wake deflection of vertical axis wind turbines by pitched blades”. In: *Wind Energy* (2023).

[32] O.M. Solomon Jr. “PSD computations using Welch’s method”. In: *NASA STI/Recon Technical Report N* 92 (1991), p. 23584.

[33] T. Kurian and J.H.M. Fransson. “Grid-generated turbulence revisted”. In: *Fluid Dynamics Research* 41 (2009), p. 021403.

[34] K.C.S. Kwok. “Turbulence effect on the flow around circular cylinder”. In: *Journal of engineering mechanics* 112 (1986), pp. 1181–1197.

[35] C.R. Kyle and E.R. Burke. “Improving the racing bicycle”. In: *Mechanical Engineering* 106.9 (1984), pp. 34–45.

[36] H. Makita. “Realization of a large-scale turbulence field in a small wind tunnel”. In: *Fluid Dynamics Research* 8 (1991), pp. 53–64.

[37] F. Malizia and B. Blocken. “Cyclist aerodynamics through time: Better, faster, stronger”. In: *Journal of Wind Engineering and Industrial Aerodynamics* 214.2 (2021), p. 104673.

[38] B.R. McAuliffe and A. D’Auteuil. “A system for simulating road-representatice atmospheric turbulence for ground vehicles in a large wind tunnel”. In: *SAE International Journal of Passenger Cars* 9.2 (2016).

[39] B.R. McAuliffe, A. Wall, and G. Larose. “Simulation of atmospheric turbulence for wind tunnel tests on full-scale light-duty vehicles”. In: *SAE International Journal of Passenger Cars* 9.2 (2016).

[40] G.L. Morrison, M.T. Schobeiri, and K.R. Pappu. “Five-hole pressure probe analysis technique”. In: *Flow measurement and instrumentation* 9 (1998), pp. 153–158.

[41] L. Mydlarski. “A turbulent quarter century of active grids : from Makita (1991) to the present”. In: *Fluid Dynamics Research* 49 (2017), p. 061401.

[42] H.J. Niemann and N. Holscher. “Cyclist aerodynamics through time: Better, faster, stronger”. In: *Journal of Wind Engineering and Industrial Aerodynamics* 33 (1990), pp. 197–209.

[43] L. Oggiano et al. “A review on skin suits and sport garment aerodynamics: guidelines and state of the art”. In: *Procedia Engineering* 60 (2013), pp. 91–98.

[44] A.E. Perry and G.L. Morrison. “Static and dynamic calibrations of constant-temperature hot-wire systems”. In: *Journal of Fluid Mechanics* 47.4 (1971), pp. 765–777.

[45] S.B. Pope. *Turbulent flows*. Cambridge University Press, 2000.

[46] P.E Roach. “The generation of nearly isotropic turbulence by means of grids”. In: *International journal of heat and fluid flow* 8.2 (1987), pp. 82–92.

[47] A. Roshko. “Experiments on the flow past a circular cylinder at very high Reynolds number”. In: *Journal of fluid mechanics* 10.3 (1961), pp. 345–356.

[48] A. Roshko. “Perspectives on bluff body aerodynamics”. In: *Journal of Wind Engineering and Industrial Aerodynamics* 49 (1993), pp. 79–100.

[49] W. Sadeh, S.P. Sutera, and P.F. Maeder. “Analysis of vorticity amplification in the flow approaching a two-dimensional stagnation point”. In: *Zeitschrift fur angewandte mathematik physik* 21 (1970), pp. 699–716.

[50] A. Spoelstra, N. Mahalingesh, and A. Sciacchitano. “Drafting effect in cycling: On-site aerodynamic investigation by the ‘Ring of Fire’”. In: *Proceedings* 49.1 (2020), p. 113.

[51] D. Telionis, Y. Yang, and O. Rediniotis. “Recent Developments in Multi-Hole Probe (MHP) Technology”. In: *20th international congress of mechanical engineering* 21 (2009).

[52] H. Tennekes and J.L. Lumley. *A First Course in Turbulence*. The Unites States of America: MIT Press, 1972.

[53] W. Terra, A. Sciacchitano, and F. Scarano. “Cyclist Reynolds number effects and drag crisis distribution”. In: *Journal of Wind Engineering and Industrial Aerodynamics* 200 (2020), p. 104143.

[54] C. Tropea, A.L. Yarin, and J.F. Foss. *Springer handbook of experimental fluid mechanics*. Heidelberg: Springer, 2007.

[55] A. Trush, S. Pospisil, and H. Kozmar. “Comparison of turbulence integral length scale determination methods”. In: *WIT Transactions on Engineering Sciences* 128 (2020), pp. 113–123.

[56] TU Delft. *W Tunnel*. 2023. URL: https://www.tudelft.nl/lr/organisatie/afdelingen/flow-physics-and-technology/facilities/low-speed-wind-tunnels/w-tunnel (visited on 02/21/2023).

[57] TU Delft Aerodynamics. *Experimental Wiki*. 2023. URL: https://wiki.tudelft.nl/bin/view/Organisation/LR/WikiAero/ExperimentalWiki/TunnelsWiki/WTunnelWiki (visited on 02/21/2023).

[58] L. Underwood and M.C. Jermy. “Fabric testing for cycling skinsuits”. In: *Procedia Engineering* 13 (2011), pp. 350–356.

[59] Union Cycliste Internationale. *UCI Cycling Regulations, Part I : General organisation of cycling as a sport*. 2023. URL: https://www.uci.org/regulations/3MyLDDrwJCJJ0BGGOFzOat#part-i-general-organisation-of-cycling-as-a-sport (visited on 02/21/2023).

[60] Union Cycliste Internationale. *UCI Cycling Regulations, Part III : Track Races*. 2023. URL: https://www.uci.org/regulations/3MyLDDrwJCJJ0BGGOFzOat#part-iii-track-races (visited on 02/21/2023).

[61] S. Watkins. “Wind-tunnel modelling of vehicle aerodynamics : with emphasis on turbulent wind effects on commercial vehicle drag”. In: *PhD Thesis* (1990).

[62] S. Watkins, B.J. Loxton, and J. Milbank. “Wind-tunnel replication of atmospheric turbulence with an emphasis on MAVs”. In: *46th AIAA Aerospace Sciences Meeting and Exhibit* 228 (2008).

[63] P. Welch. “The use of fast fourier transform for the estimation of power spectra : a method based on time averaging over short, modified periodograms”. In: *IEEE Transactions on audio and electroacoustics* 15.2 (1967), pp. 70–73.

[64] J. Westerweel, B.J. Boersma, and F.T. Nieuwstadt. *Turbulence: Introduction to Theory and Applications of Turbulent Flows*. Springer International Publishing, 2016.

[65] M.M. Zdravkovich. “Conceptual overview of laminar and turbulent flows past smooth and rough cylinders”. In: *Journal of Wind Engineering and Industrial Aerodynamics* 33 (1990), pp. 53–62.

A

Velodrome Results

A.1. Time series

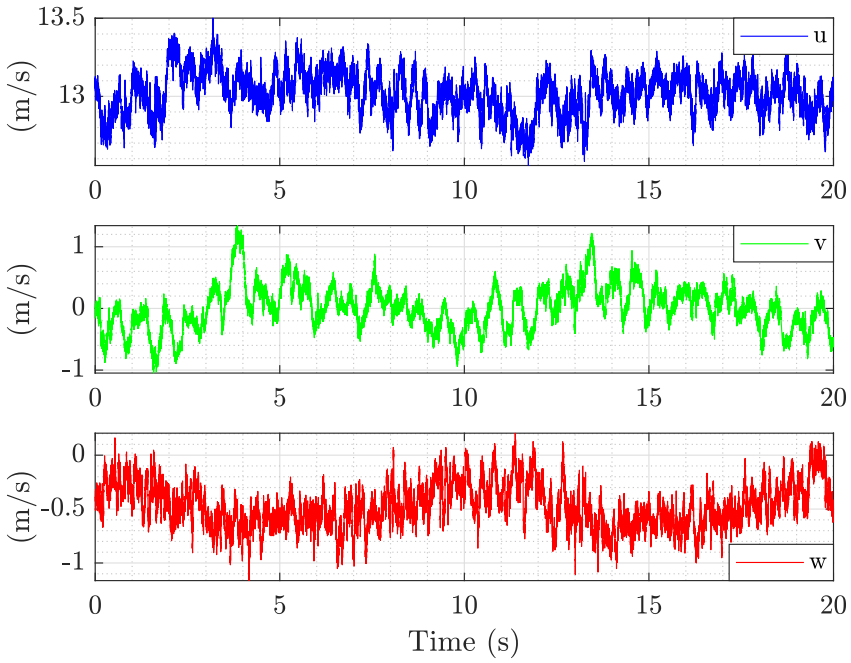

Figure A.1: Variation of the velocity components with time over the course of a single lap

A.2. Turbulence measured at varying rider speeds

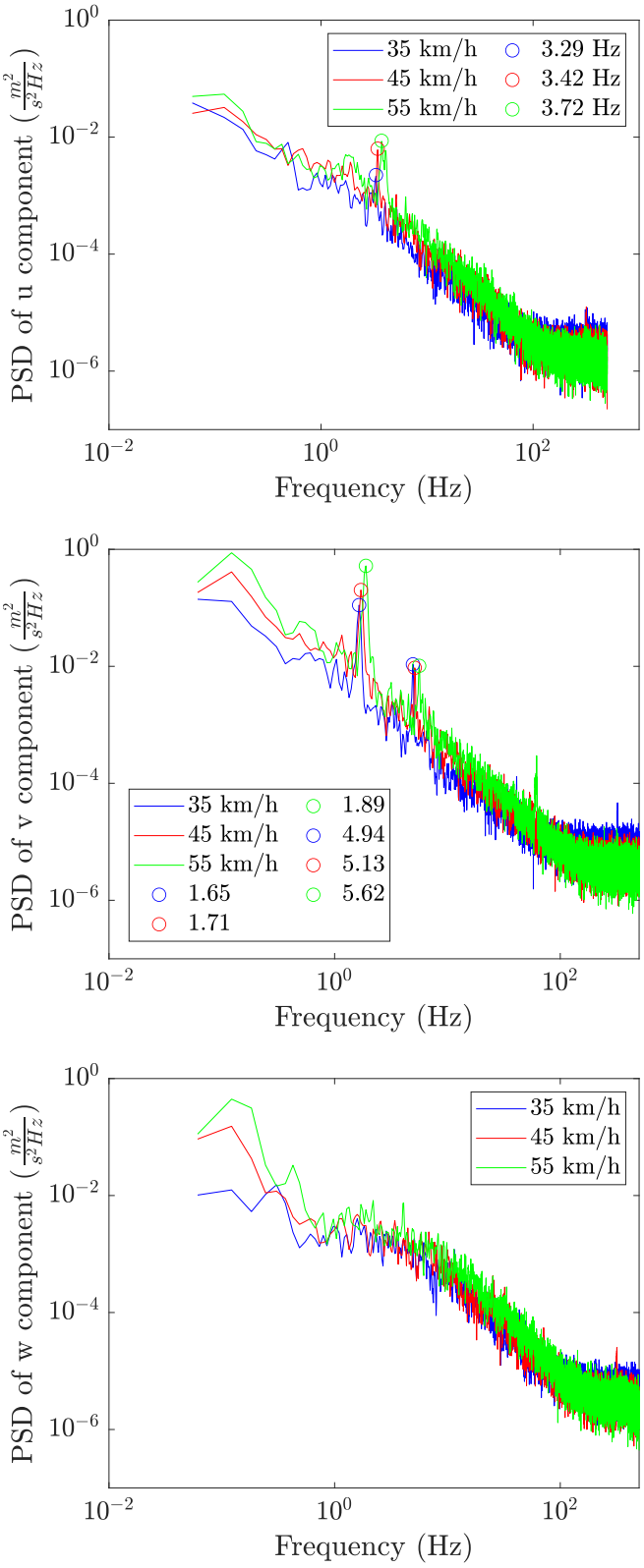

Figure A.2: Comparison of PSD of the u, v, w components of velocity at different rider velocities

A.3. Turbulence encountered by a trailing cyclist

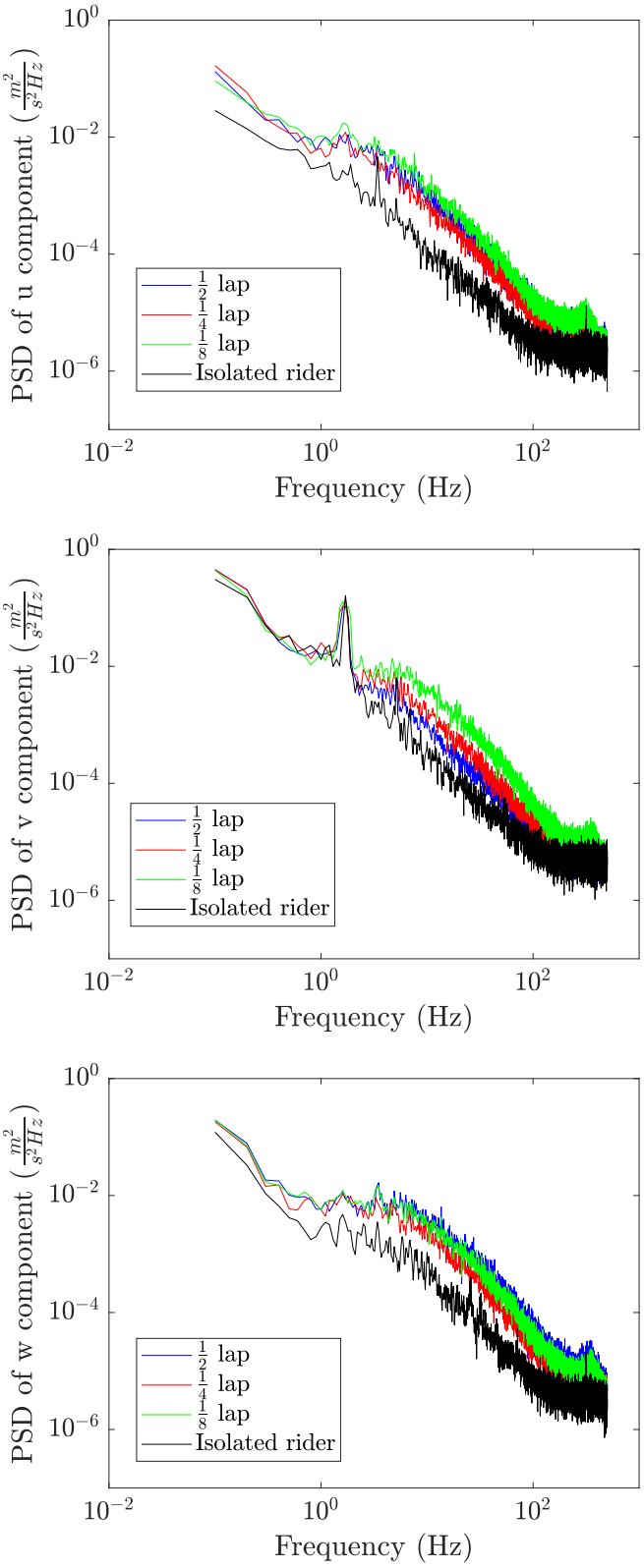

Figure A.3: Comparison of PSD of the u, v, w components of velocity at different separation distances

B

Wind tunnel results

B.1. Turbulence simulation

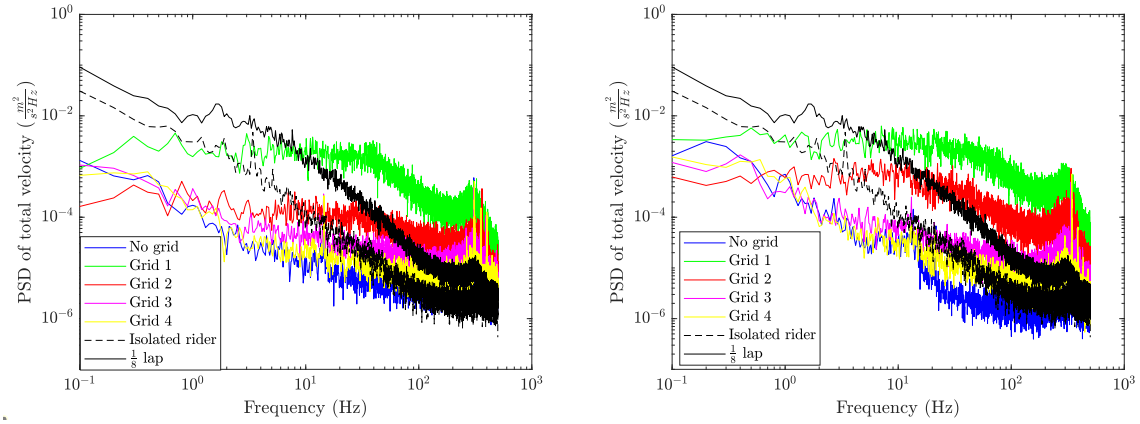

Figure B.1: A comparison of turbulence spectra obtained from Grid 1, 2, 3, 4 with the lower and upper levels of turbulence measured in a velodrome at a rider speed of 12.5 m/s. On the left is the spectra obtained at a wind tunnel velocity of 10 m/s, and on the right are spectra obtained at a wind tunnel velocity of 15 m/s. Also included is the turbulence of the wind tunnel in the absence of grids

B.2. Drag measurements

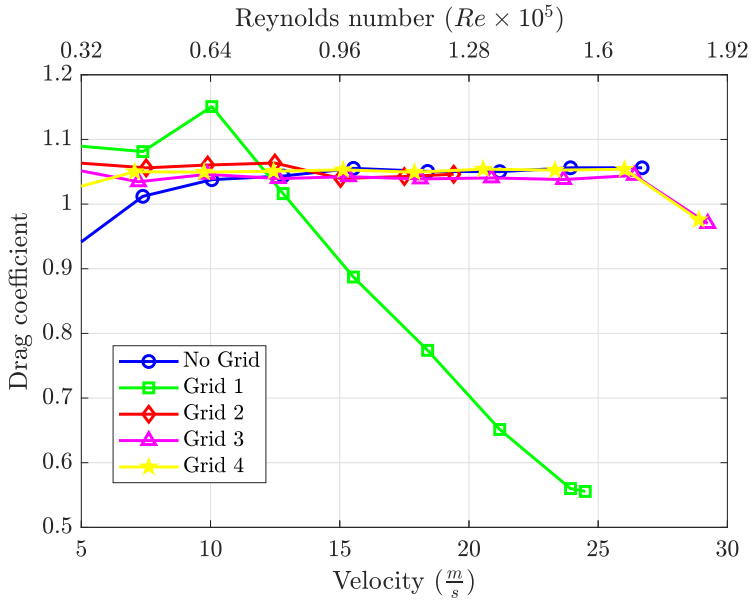

Figure B.2: Drag coefficient vs Velocity, Reynolds number for a smooth surfaced cylinder under turbulent flow generated by Grids 1, 2, 3 and 4

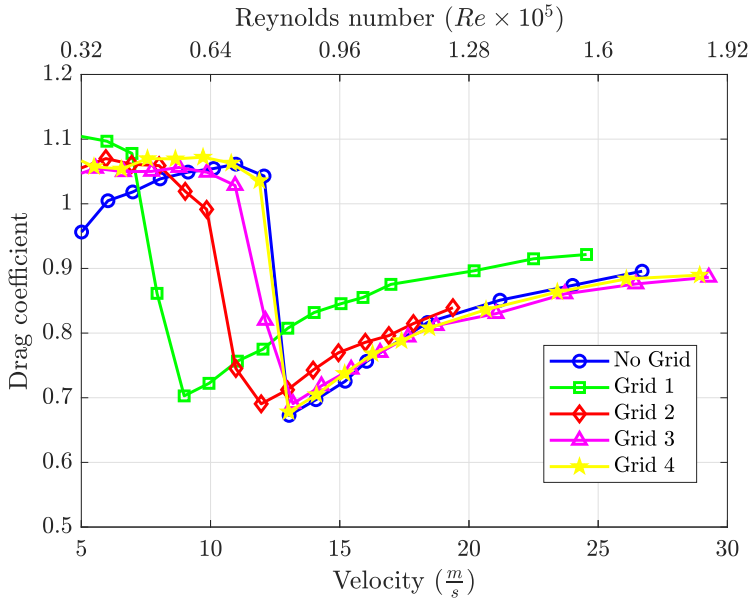

Figure B.3: Drag coefficient vs Velocity, Reynolds number for a rough surfaced cylinder under turbulent flow generated by Grids 1, 2, 3 and 4